J. Fluid Mech. (1997), *vol.* 335, *pp.* 261–304

Computation of jet mixing noise due to coherent structures: the plane jet case

By F. BASTIN[1], P. LAFON[2] AND S. CANDEL[3]

[1]SNECMA, Centre de Villaroche, 77550 Moissy-Cramayel, France

[2]Département Acoustique et Mécanique Vibratoire, EDF, 1 Avenue du Général de Gaulle, 92141 Clamart Cedex, France

[3]EM2C Laboratory, CNRS, Ecole Centrale Paris, 92295 Châtenay-Malabry Cedex, France

(Received 8 June 1995 and in revised form 21 October 1996)

A computational approach to the prediction of jet mixing noise is described. It is based on Lighthill's analogy, used together with a semi-deterministic modelling of turbulence (SDM), where only the large-scale coherent motion is evaluated. The features of SDM are briefly illustrated in the case of shear layers, showing that suitable descriptions of the mean flow and of the large-scale fluctuations are obtained. Aerodynamic calculations of two cold fully expanded plane jets at Mach numbers 0.50 and 1.33 are then carried out. The numerical implementation of Lighthill's analogy is described and different integral formulations are compared for the two jets. It is shown that the one expressed in a space–time conjugate (κ, ω)-plane is particularly convenient and allows a simple geometrical interpretation of the computations. Acoustic results obtained with this formulation are compared to relevant experimental data. It is concluded that the radiation of subsonic jets cannot be explained only by the contribution of the turbulent coherent motion. In this case, directivity effects are well recovered but the acoustic spectra are too narrow and limited to the low-frequency range. In contrast at Mach number 1.33, especially in the forward quadrant, results are satisfactory, showing that coherent structures indeed provide the main source of supersonic jet mixing noise.

1. Introduction

Sound generated by turbulence raises many questions of fundamental and technical interest, which have been extensively investigated in the past forty years. While the initial effort was essentially analytical and experimental, recent work has relied more heavily on computational techniques. The problem is indeed difficult since the noise originates in turbulent fluctuations which show a very wide range of spatial and temporal frequencies, and complete knowledge of the flow field is still out of reach for configurations of practical interest. Thus a steady statistical description of the turbulent flow has long been used as in the work of Ribner (1969) or Goldstein & Rosenbaum (1973). These authors employed analytical turbulence models and more recently Béchara *et al.* (1995) combined a similar formulation with results obtained from numerical simulations. Interesting features of the noise production mechanism have been obtained but this approach, which does not distinguish different turbulent scales, suffers a few limitations regarding its generality. This is why we are interested

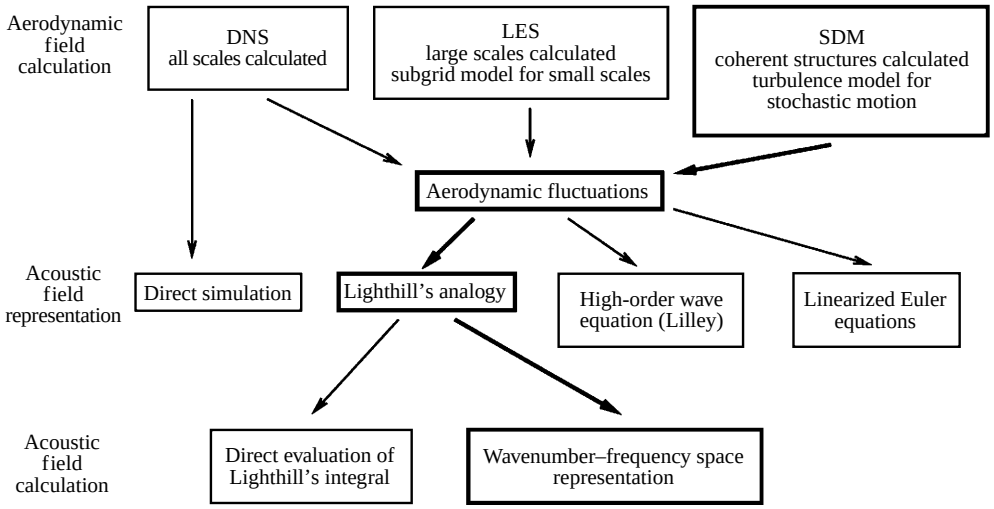

FIGURE 1. From turbulent fluctuations to the radiated noise. The path chosen here is indicated with bold rules.

here in techniques involving the use of a time-dependent representation of the flow field.

To provide the proper background to the present investigation, we show in figure 1 the main routes which may be taken to evaluate the sound field generated by turbulent fluctuations. For the computation of the aerodynamic field a choice has to be made between direct numerical simulation (DNS), large-eddy simulation (LES) or semi-deterministic modelling (SDM), the latter pertaining, as detailed below, to the family of unsteady Reynolds averaged Navier–Stokes simulations (RANS). One then has to introduce an acoustic field representation which may be based on Lighthill's analogy, higher-order wave equations or the linearized Euler set of equations. Each of these descriptions includes an identification of the acoustic source term. The sound field may then be evaluated in various ways. Among the many possible paths, we investigate in this article one combination. However the methodology which is developed here can be used equally to investigate other possible choices. As shown in figure 1 the classical theory devised by Lighthill in 1952 constitutes a key approach, where the problem of sound emission by turbulent flow is shown to be equivalent to the radiation in free space of a source term representing the turbulent aerodynamic fluctuations. The theory has the only fundamental limitation of implying a separation between the source volume of the aerodynamic field and the far region where the acoustic field propagates. In particular the interaction between acoustic propagation and the mean flow, that is refraction, cannot be taken directly into account. Yet Lighthill's aeroacoustic analogy is a powerful and general approach based on a limited set of assumptions. One purpose of this paper is to investigate the use of this classical theory in computational aeroacoustics (CAA), with the objective of obtaining a numerical prediction of jet mixing noise.

For the computation of the turbulent flow, direct numerical simulation may be applied to simple configurations of fundamental interest (see e.g. Mitchell, Lele & Moin 1995) but is still far from addressing the range of Reynolds numbers that have to be dealt with in practice. An intermediate approach may be devised by considering the large-scale motion in the turbulent flow and calculating the acoustic

field resulting from these fluctuations only. It is known from the work of Brown & Roshko (1974) that large-scale coherent structures exist in shear layers and it has since been recognized that these structures are an essential feature of free shear flows even at high Reynolds number. In the field of aeroacoustics, the question immediately arose of the relation between these coherent structures and the radiated noise field, or more precisely of the contribution of the coherent part of the turbulence to the acoustic field (Laufer 1974). In 1971, Crow & Champagne had had the idea that jet noise could be modified by acting on the orderly part of the flow. At the same time, Bishop, Ffowcs Williams & Smith (1971) postulated that for supersonic jets the principal noise sources were very large-scale wave-like undulations of the jet flow. Three years later, Liu (1974), in a study that contains several basic ideas of the present paper, considered a triple decomposition of turbulence, one of its components being an instability wave field representing the organized part of turbulence, the amplitude of which was determined by a kinetic energy equation. The near-jet noise field was eventually calculated from the 'large-scale wave-like eddies' while the fine-grained turbulent fluctuations were modelled.

In fact, Liu's theory was tested for jet exit Mach numbers between 1.27 and 1.67 and it is now agreed that supersonic jet mixing noise is controlled by large-scale organized turbulence. The physical mechanism underlying this statement is the 'Mach wave' phenomenon: a turbulent eddy convected at supersonic speed produces a strong and directive acoustic radiation at the Mach wave angle (see e.g. Ffowcs Williams & Maidanik 1965; Phillips 1960). With a wave-like point of view, only an instability wave – which may be the basis of the representation of organized turbulence – with supersonic convection velocity radiates noise, a fact emphasized by Tam & Morris (1980). The spatial growth and decay of instability waves being taken into account, supersonic convection velocities may be expected in axisymmetric jets for supersonic or high subsonic exit Mach numbers. Thus, many experiments, for example by McLaughlin, Morrison & Troutt (1975, 1977) or Seiner, McLaughlin & Liu (1982) show that the acoustic spectra measured for fully expanded supersonic jets are not deeply modified when the Reynolds number is varied, which substantiates the theory that fine-scale turbulence does not contribute significantly to the noise radiated, essentially by a low-level broadband signal. On the theoretical side various jet noise models based on the same hypothesis were proposed by Morris (1977), Ffowcs Williams & Kempton (1978) and Tam & Morris (1980), and applied to supersonic jets. Further studies like Tam & Burton (1984) have left little doubt that experimental supersonic jet mixing noise data can be explained well in terms of the contribution of large-scale coherent structures only.

In contrast the question remains to be settled in the subsonic range, where theoretical analyses are ambiguous and experimental results inconclusive. For example Moore (1977) obtains a broadband amplification of the turbulence and radiated noise proportional to the excitation of a subsonic jet, but observes no enhancement of the large-scale motion, which leads him to conclude that the direct radiation of the large-scale instabilities is negligible. On the other hand, Laufer & Yen (1983) excite the initial laminar shear layer of a subsonic jet and report a reduction of the broadband acoustic radiation. On the basis of high correlation levels of the radiated noise with shear layer instabilities, they state that the growth and saturation of these instabilities is a major noise contributor. In this context it is admitted (Tam 1991) that analytical or numerical results are not yet available to provide a definitive answer to the question.

In this article, we would like to address these issues from a numerical standpoint through the study of two plane jet flows at Mach number 0.50 and 1.33. Present jet noise calculations rely on the computation of coherent structures only. For that, following Ha Minh's suggestion (Ha Minh 1994), a semi-deterministic turbulence modelling is used, where coherent turbulence fluctuations are computed while the stochastic fluctuations are modelled. The radiated noise is then computed from Lighthill's analogy. It must be noted here that this approach is computational at two different levels: the evaluation of Lighthill's source term which appears as a computational fluid dynamics (CFD) problem and the treatment of Lighthill's integral which is rather a specific computational aeroacoustics (CAA) matter. The ambition of this paper is to bring to light and as far as possible to treat the specific problems connected with this choice. Moreover, we here consider classical ideas concerning jet mixing noise processes to build a numerical prediction tool. Thus we try to refer as often as possible to relevant theoretical work available and ultimately to experimental data.

In principle the calculations of the turbulent flow field and the radiated sound should be carried out in three dimensions. In what follows, the large-scale motion is computed in two dimensions while the fine-grained turbulence is treated with a three-dimensional model and the acoustic field is also evaluated in three dimensions. It is well known that the large-scale motion may feature three-dimensional characteristics but at this point in time the computational resources required for a fully three-dimensional computation are not available. This is certainly a limitation of the present analysis but it has been shown in the past that much could be learnt from two-dimensional models. Moreover the dominant organized motion in free shear flows is often structured around two-dimensional spanwise vortices, especially here in plane jets with the shear layer convective Mach number well below 1. Finally it seems to us unlikely that the main conclusions presented herein would be affected by the three-dimensionality of the flow large scales.

In §2, the semi-deterministic modelling (SDM in the following) is presented. This model is a modified $k-\epsilon$ turbulence closure. SDM is tested in the two-dimensional shear layer configuration with special attention given to the energy balance between the deterministic and random turbulence components. The plane jet flow computations using SDM are described in §3. Section 4 is devoted to the numerical implementation of Lighthill's analogy. It is shown that, in agreement with existing theoretical studies, the choice of a formulation of the theory adapted to numerical evaluation is crucial, especially for subsonic jets. The appropriate formulation is the one expressed in the conjugate $(\boldsymbol{\kappa}, \omega)$ space, which yields an interesting geometrical interpretation of the calculations, where the jet convection Mach number appears as an essential parameter. The analysis of the acoustic results with respect to known experimental data is the subject of §5, paying particular attention to their ability to give reliable subsonic jet mixing noise predictions considering only the contribution of large-scale coherent structures. This article concludes briefly with a few prospective remarks (§6).

2. The semi-deterministic modelling (SDM)

2.1. *The turbulence triple decomposition*

While the existence of 'coherent structures' in shear flows is substantiated by many observations, extraction of the coherent component poses problems. Experimentally

the most common approach is to extract the coherent fluctuations by taking phase or conditional averages using a phase reference either given by an external excitation or by the detection of a specific event in the flow (Crow & Champagne 1971; Lepicovsky *et al.* 1985). The theoretical version consists of using conditional ensemble averaging, as opposed to time averaging which is obviously not relevant in the extraction of the coherent motion. For simplicity consider a flow submitted to periodic forcing. The phase average of a fluctuating quantity may be defined as

$$\overline{\Phi}(\boldsymbol{y},t) = \lim_{N\to\infty} \frac{1}{N} \sum_{i=1}^{N} \Phi_i(\boldsymbol{y},t),$$

where $\Phi_i(\boldsymbol{y},t)$ stands for $\Phi(\boldsymbol{y},t+i\tau)$ and τ is the period of the forcing. In the absence of such a simple forcing, which easily provides a phase-locking of the flow, the conditional ensemble average $\overline{\Phi}(\boldsymbol{y},t)$ must be seen as a generalization of the phase average and is denoted likewise. $\Phi_i(\boldsymbol{y},t)$ may then be interpreted as a realization i of the flow. It is now possible to define the incoherent fluctuations of Φ as

$$\Phi'(\boldsymbol{y},t) = \Phi(\boldsymbol{y},t) - \overline{\Phi}(\boldsymbol{y},t)$$

and if $\langle\Phi\rangle$ denotes the classical time average of Φ, the coherent fluctuations are determined by

$$\Phi_c(\boldsymbol{y},t) = \overline{\Phi}(\boldsymbol{y},t) - \langle\Phi\rangle(\boldsymbol{y}).$$

These considerations lead to the triple decomposition of the turbulent field made explicit by Hussain & Reynolds (1970):

$$\Phi(\boldsymbol{y},t) = \underbrace{\langle\Phi\rangle(\boldsymbol{y}) + \Phi_c(\boldsymbol{y},t)}_{\overline{\Phi}(\boldsymbol{y},t)} + \Phi'(\boldsymbol{y},t).$$

The turbulent flow field is formally split into three parts: the mean flow or time-averaged flow, the coherent fluctuating flow and the incoherent or stochastic fluctuating flow. The use of such a decomposition in studies of turbulent shear flows is not new. It had been suggested in early articles by Liepmann (1952). This kind of splitting in terms of organized large-scale structures and fined-grained turbulence was explored further by Hussain & Reynolds (1970), Liu (1974), and by many other authors interested in the analysis of turbulent shear flows (see Liu 1988 for an extensive discussion). The objective is in any event to stress the distinction between deterministic large-scale coherent motion and stochastic turbulence.

The basic idea of SDM is to recognize this distinction between aerodynamic fluctuations that are strongly determined by the features of the mean flow and smaller eddies, coming from the Kolmogorov cascade of these coherent structures. The nature of the small-scale stochastic fluctuations is believed to be universal and similar to the traditional turbulence concept. It is then legitimate to suppose that coherent structures (represented by Φ_c) are predictable and may be computed, while incoherent fluctuations (Φ') may be represented by their statistical properties with the help of a turbulence model. This technique, which has been investigated by different authors (Ha Minh *et al.* 1989; McInnes, Claus & Huang 1989; Johansson, Davidson & Olsson 1993), is the basis of the present flow computations.

It must not be forgotten that the triple decomposition originates from experimental observations and that the coherent aerodynamic field is supposed to represent the large-scale turbulent structures. Consequently it must be possible to compute $\overline{\Phi}$ on a grid much coarser than that necessitated by direct numerical simulations (DNS). In

this respect, SDM is similar to large-eddy simulation (LES), a technique which could have been used as well in this study. Yet, these two approaches are fundamentally different. In LES, a spatial averaging is performed by convoluting the flow variables with a low-pass filter. The width of this filter sets the position of the limit between the low-frequency components of the spatial spectrum which are calculated and the remaining high-frequency components which are modelled. With SDM there is no such clear and adjustable cut-off, which makes it in principle less flexible and predictable. On the other hand SDM has some important advantages that must be stressed. The statistical average (or ensemble average) used to define the triple decomposition forms the basis of traditional turbulence modelling, despite the fact that in this case statistical and time averages are generally mixed up. This means that classical and well-known turbulence models may be used for SDM. Yet, these classical models were usually adjusted for configurations, such as grid turbulence, where coherent structures are insignificant. Thus SDM requires a recalibration of the turbulence model.

Ha Minh (1994) suggests that the $k-\epsilon$ turbulence model, initially derived by Jones & Launder (1972), can be used to describe the fine-grained turbulence. For more clarity, let us briefly recall the essential features of this model, presented here in its compressible version.

Mass averaging, denoted $\tilde{\Phi}$, must be introduced:

$$\tilde{\Phi} = \overline{\rho\Phi}/\overline{\rho},$$

where ρ is the density. The associated decomposition is

$$\Phi = \tilde{\Phi} + \Phi''.$$

With this definition, the compressible Navier–Stokes equations may be cast into a form very similar to the incompressible version.

The fine-grained turbulence model is based on the eddy viscosity concept, where the Reynolds stress is approximated by

$$-\overline{\rho u_i'' u_j''} = \mu_t \left(\frac{\partial \tilde{u}_i}{\partial y_j} + \frac{\partial \tilde{u}_j}{\partial y_i} - \frac{2}{3}\delta_{ij}\frac{\partial \tilde{u}_l}{\partial y_l} \right) - \tfrac{2}{3}\delta_{ij}\overline{\rho}k. \tag{2.1}$$

Here k is the turbulent kinetic energy $\overline{\rho u_i'' u_i''}/2\overline{\rho}$ and μ_t is the turbulent viscosity. Note that k represents the turbulence associated with modelled stochastic small scales only. For comparisons with experimental measurements of the turbulence level, it is necessary to also include the contribution of the resolved coherent fluctuations. This point is illustrated below.

In the $k-\epsilon$ model, the turbulent viscosity is determined by

$$\mu_t = C_\mu \overline{\rho}\frac{k^2}{\epsilon},$$

where C_μ is an empirical constant, traditionally equal to 0.09, and ϵ is the turbulent kinetic energy dissipation rate. The balance equations of the compressible $k-\epsilon$ model are well-known and will not be reproduced here. It is sufficient to mention that this two-equation model together with the Navier–Stokes system (including continuity, momentum and energy conservation) forms a closed system. Observing that the standard model tends to overestimate the turbulence production in high-shear regions, where coherent structures are likely to emerge, Ha Minh (1994) proposes reducing the value of C_μ, thus decreasing the turbulent viscosity, to build the SDM. For example for the backward facing step case he obtains the optimal value $C_\mu = 0.02$.

It is also indicated that C_μ is not universal and should be adjusted for each flow configuration, whereas it was set to a unique value in the original model. This is why in the following sections we test SDM on the well-documented shear layer configuration with C_μ at its standard 0.09 value (§2.2) before observing the effect of a modification of this constant. It is shown in §2.3 that decreasing C_μ essentially results in shifting the energy balance between coherent and incoherent motion (§2.3) in the sense of increasing the coherent structures level. Jet computations presented later (§3) are performed with $C_\mu = 0.05$.

At this point one may wonder if SDM may properly describe the interaction between the coherent and fine-scale parts of the unsteady flow. This interaction is accounted for by the eddy viscosity concept of the turbulence model, which like any model is a simplified representation of the incoherent turbulent stresses, but has been shown to be a suitable compromise between complexity and accuracy. The eddy viscosity concept is also widely used for LES subgrid-scale models, which also aim at representing the interaction between large-scale and fine-grained turbulent fluctuations.

One may also doubt that coherent and incoherent motions may be treated as uncorrelated. This point, while certainly questionable in principle, is quite reasonable. We discuss here time correlation and the characteristic time scales of both types of fluctuations are of a different order of magnitude. As underlined by Hussain (1983), the coupling of coherent and incoherent motions by energy transfer does not imply that they are correlated. Besides, the experimental characterization of coherent structures consisting as mentioned above in exciting the flow and extracting the fluctuations correlated with this excitation relies on this assumption.

Finally we would like to defend the approach followed in the paper. It is not assumed that SDM provides a definitive solution to the problem at hand. This is why we feel it necessary to include calculations performed on the shear layer test case (§2.2). The validations of the next subsection will establish with confidence that the model allows a realistic computation of the deterministic part of the turbulent fluctuations.

2.2. *Test on the shear layer*

The plane mixing layer (see figure 2) is a basic shear flow, for which many theoretical and experimental results exist. Thus, it constitutes a relevant test case before dealing with jet flows. One of its essential properties is the absence of a characteristic length scale. Only a velocity scale, for example the half-sum U_M of the free-stream speeds U_a and U_b, is readily available. Thus, after the distance required to 'forget' initial conditions specified at the confluence, the statistical properties of the flow are self-similar in the variables y_2/y_1, y_1 and y_2 being respectively the streamwise and transverse coordinates.

This leads to different verifications of SDM calculations. The similarity of time-averaged profiles implies that the shear layer thickness δ must grow linearly with y_1. The shear layer growth inferred from the slope of the curve $\delta(y_1)$ is a characteristic parameter of the flow and may be compared to experimental data. The similarity of various statistical moments of the flow may be checked. The mean streamwise velocity and turbulence intensity profiles are examined in this test. Finally the peak frequency of the velocity fluctuations scales with $1/y_1$, and may be estimated with a linear stability approach.

Results are presented for three mixing layers with various combinations of supersonic and subsonic flow. The three cases are defined in table 1. The subscript a

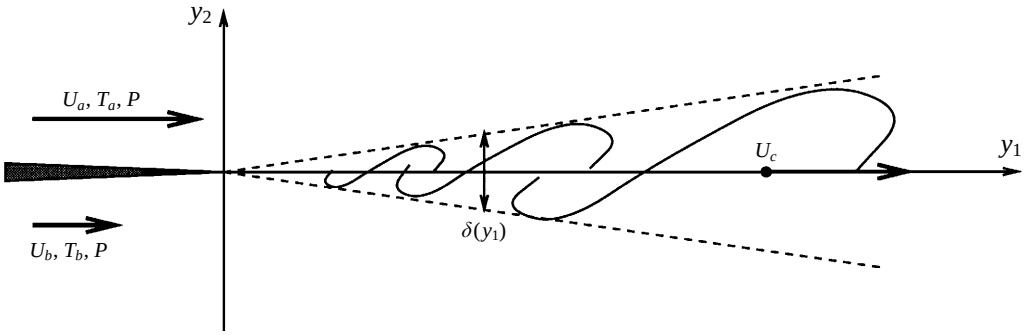

FIGURE 2. The plane mixing layer.

Case	M_a	M_b	T_a (K)	T_b (K)	P (Pa)	$r = U_b/U_a$	$s = \rho_b/\rho_a$	M_c
Shear layer 1	0.7	0.3	273	295	1.08×10^5	0.45	0.93	0.19
Shear layer 2	3.1	1.7	137	253	2.35×10^3	0.75	0.54	0.33
Shear layer 3	1.8	0.5	177	277	5.46×10^4	0.35	0.64	0.52

TABLE 1. Main characteristics of the three shear layers

(respectively b) refers to the free stream in the region $y_2 > 0$ (respectively $y_2 < 0$), M is the Mach number, U the velocity, T the temperature and P the pressure, identical in the two streams. The parameters $r = U_b/U_a$ and $s = \rho_b/\rho_a$ are indicated together with the convective Mach number

$$M_c = \frac{\Delta U}{c_a + c_b},$$

where $\Delta U = |U_a - U_b|$ and c is the speed of sound. The mixing layers 2 and 3 were investigated respectively by Papamoschou & Roshko (1988) and Samimy & Elliott (1990).

2.2.1. *Numerical method*

The SDM equations with $C_\mu = 0.09$ are advanced in time with an explicit McCormack scheme (McCormack 1981). This scheme is second-order accurate in space and time, and is suited for unsteady computations. The Courant–Friedrichs–Lewy number (CFL) is taken equal to 0.9. No artificial viscosity is used besides the low inherent dissipation of the scheme. The Cartesian two-dimensional grid is stretched from the extremity of the splitter plate in both y_1- and y_2-directions, and is defined in table 2. The splitter plate itself is not included in the computational domain, and is represented via the inflow profiles. All variables are imposed at the inflow, with constant density and temperature on each side of the shear layer origin, and constant pressure throughout the inflow. Two laminar boundary layer velocity profiles with same momentum thickness $\delta_{\theta 0}$ are prescribed on each side of the splitter plate, the tip of which is simulated by one node with zero velocity. The Reynolds number $Re = U_a \delta_{\theta 0}/\mu_a$ is 2 000. Finally, constant profiles are given for k and ϵ, with $k = (0.002\, U_a)^2$ and $\epsilon = \rho_a k^2/\mu_a$, but it has already been reported, and observed again here, that these initial values can be varied by several orders of magnitude with negligible impact on the established solution. For the shear layer case it is

Direction	Domain size	Number of points	Δy_{min}	Δy_{max}	Grid stretching
y_1	7 500 (15 000)	180 (232)	10	110 (220)	1.3%
y_2	3 000 (6 000)	100 (123)	5	95 (187)	3.0%

TABLE 2. The shear layer computational grid. All dimensions are expressed in terms of the initial momentum thickness $\delta_{\theta 0}$. Data are given for the physical part of the computational domain, and when between parenthesis for the complete domain (including the dissipation zone).

not necessary to introduce any time-dependent forcing: prescribed inflow profiles are steady. In this respect and as discussed further below, the jet case is different.

As prescribed in Colonius, Lele & Moin (1993), the computational domain is extended in the streamwise direction and on the sides by an artificial absorption layer which progressively damps disturbances to make the boundary conditions treatment easier. As may be seen from table 2 the complete domain including this dissipation layer is exactly twice the size in both directions of the physical part of the domain alone. The grid stretching is continuous all across the complete domain. In the following only the flow computed in the physical domain is presented. Neumann conditions are applied on the lateral boundaries. Finally characteristics-based non-reflecting outflow boundary conditions discussed by Poinsot & Lele (1992) are implemented at the outflow. The combination of a dissipation layer with high-quality boundary conditions shows excellent performance at moderate cost and seems at the present time the best way to handle unsteady compressible computations of free shear flows.

It may be pointed out here that Lighthill's theory basically requires knowledge of the turbulent flow. It is not necessary to accurately represent the propagation of acoustic waves over many wavelengths, which would demand a significantly larger computational effort.

With these practical conditions, figure 3 shows an instantaneous view of each shear layer. The passive scalar field has been chosen as it allows clear visualizations of the large-scale structures which are of special interest here. The similarity with experimental shadowgraphs is striking. The view is taken long after the first structure has been convected out of the calculation domain, so that the flow is fully developed. This takes a time $t_0 = L/U_c$ where L is the domain length and U_c the structures convection speed. In the shear layer, U_c may be estimated as (see e.g. Dimotakis 1986)

$$U_c = \frac{U_a c_b + U_b c_a}{c_a + c_b}.$$

2.2.2. *The growth rate*

The local vorticity thickness δ_ω is estimated as

$$\delta_\omega = \frac{\Delta U}{|\partial \langle \tilde{u}_1 \rangle / \partial y_2|_{max}}.$$

Two points concerning the time average are worth noting. First, the traditional expression for δ_ω contains $\langle u_1 \rangle$, which has been replaced here by $\langle \tilde{u}_1 \rangle$. But it is straightforward to find out that for any variable Φ

$$\langle \tilde{\Phi} \rangle - \langle \Phi \rangle = \langle \tilde{\Phi} \rangle - \langle \overline{\Phi} \rangle = \left\langle \frac{\overline{\rho' \Phi'}}{\overline{\rho}} \right\rangle$$

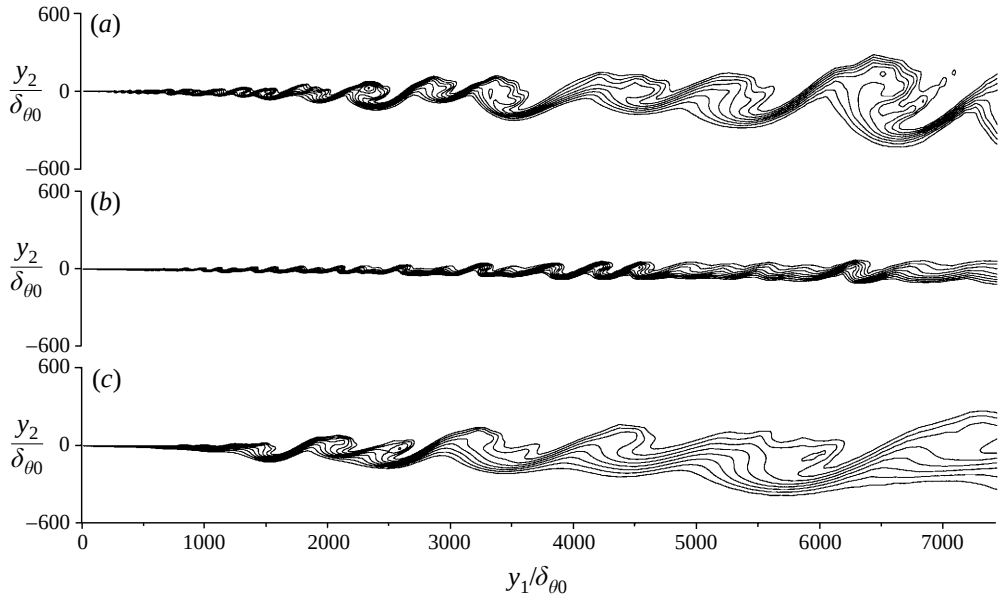

FIGURE 3. Instantaneous passive scalar field for the three shear layer computations. (*a*) Case 1 ($M_c = 0.19$); (*b*) case 2 ($M_c = 0.33$); (*c*) case 3 ($M_c = 0.52$). The passive scalar is initialized at 0 in the region $y_2 < 0$ and 1 in $y_2 > 0.8$ contours are drawn from 0.15 to 0.85 in increments of 0.10.

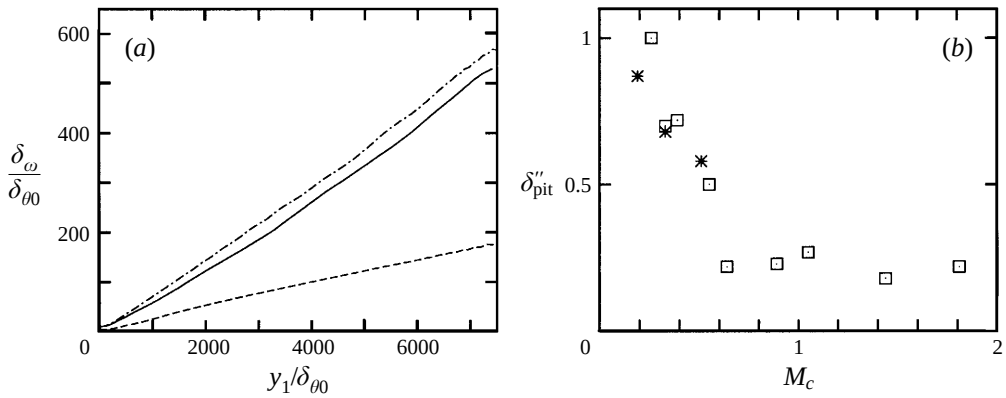

FIGURE 4. Development of the shear layers. (*a*) Vorticity thickness δ_ω: ——, case 1 ($M_c = 0.19$); – – – –, case 2 ($M_c = 0.33$); — · —, case 3 ($M_c = 0.52$); all distances are reduced by the initial momentum thickness. (*b*) Reduced Pitot growth rates δ''_{pit} with respect to convective Mach number M_c: open squares correspond to data of Papamoschou & Roshko (1988); stars indicate present calculations.

so that

$$\left| \frac{\langle \tilde{\Phi} \rangle - \langle \Phi \rangle}{\langle \Phi \rangle} \right| \leqslant \left[\left\langle \frac{\overline{\rho'^2}}{\overline{\rho}^2} \right\rangle \frac{\langle \overline{\Phi'^2} \rangle}{\langle \Phi \rangle^2} \right]^{1/2},$$

from which it is possible to assume that $\langle \tilde{\Phi} \rangle \approx \langle \Phi \rangle$. Also it is important to ensure statistical stability of the average values. This is achieved well by starting the averaging at time t_0 and summing over a total time exceeding $3t_0$.

The evolution of δ_ω along the streamwise direction is represented in figure 4(a) for the three cases. It is possible to verify that the flow grows linearly. For case 3, the value of the vorticity growth rate

$$\delta'_\omega = \frac{\mathrm{d}\delta_\omega}{\mathrm{d}y_1}$$

obtained from the present curve, that is 0.075, is close to the experimental value of 0.079 given by Samimy & Elliott (1990). More generally, different authors (e.g. Bogdanoff 1983; Papamoschou & Roshko 1988) have shown that the convective Mach number M_c characterizes compressibility, so that the growth rate scaled by its 'incompressible value' is a function of M_c only. The normalized Pitot growth rates δ''_{pit} are plotted in figure 4(b) for the three shear layers along with the experimental data of Papamoschou & Roshko (1988). The Pitot thickness δ_{pit} is defined as the difference between the two transverse locations where the total pressure (or Pitot pressure) differs by 5% from its asymptotic value on each side of the mixing layer. The incompressible Pitot growth rate is estimated by Papamoschou & Roshko (1988) as

$$\delta'_{pit,0} = 0.14\,\frac{(1-r)(1+s^{1/2})}{1+r\,s^{1/2}}$$

and by definition the normalized Pitot growth rate is

$$\delta''_{pit} = \frac{\delta'_{pit}}{\delta'_{\mathrm{pit},0}}.$$

The three numerical points follow reasonably well the experimental trend, taking into account that the experimental accuracy is 10% for the growth rate measurements. For case 2, where the comparison is direct since the numerical and experimental shear layers are the same, the two corresponding points are nearly superposed.

One may note from figure 3 or 4(a) that the absolute growth rate of the second shear layer (case 2) is much lower than the two others (cases 1 and 3). This is due to the high value of the velocity ratio for this case. On the other hand the reduced growth rates δ''_{pit}, where compressibility effects are corrected for, are decreasing in the order case 1, 2 and 3 (see figure 4b), in agreement with experimental observations. Compressibility effects are thus well captured by the computation.

2.2.3. *Self-similarity*

Similarity profiles of the streamwise velocity are shown in figure 5 (a,b,c). It is possible to verify that self-similarity has already been achieved at $y_1/\delta_{\theta 0} = 1000$ for cases 1 and 3 while it is necessary to reach $y_1/\delta_{\theta 0} = 2500$ for case 2. Anyway, it is always attained long before the end of the computational domain.

Before considering the streamwise turbulence self-similarity, a delicate problem must be pointed out. The experimental definition of streamwise turbulence is based on the r.m.s. velocity fluctuations:

$$\sigma_1 = (\langle u_1^2\rangle - \langle u_1\rangle^2)^{1/2}.$$

It is not possible to identify this quantity with the r.m.s. velocity fluctuations that are computed using SDM where only coherent fluctuations are calculated. In fact, $u_1 = \tilde{u_1} + u''_1$ and as explained above, the coherent and incoherent motions are

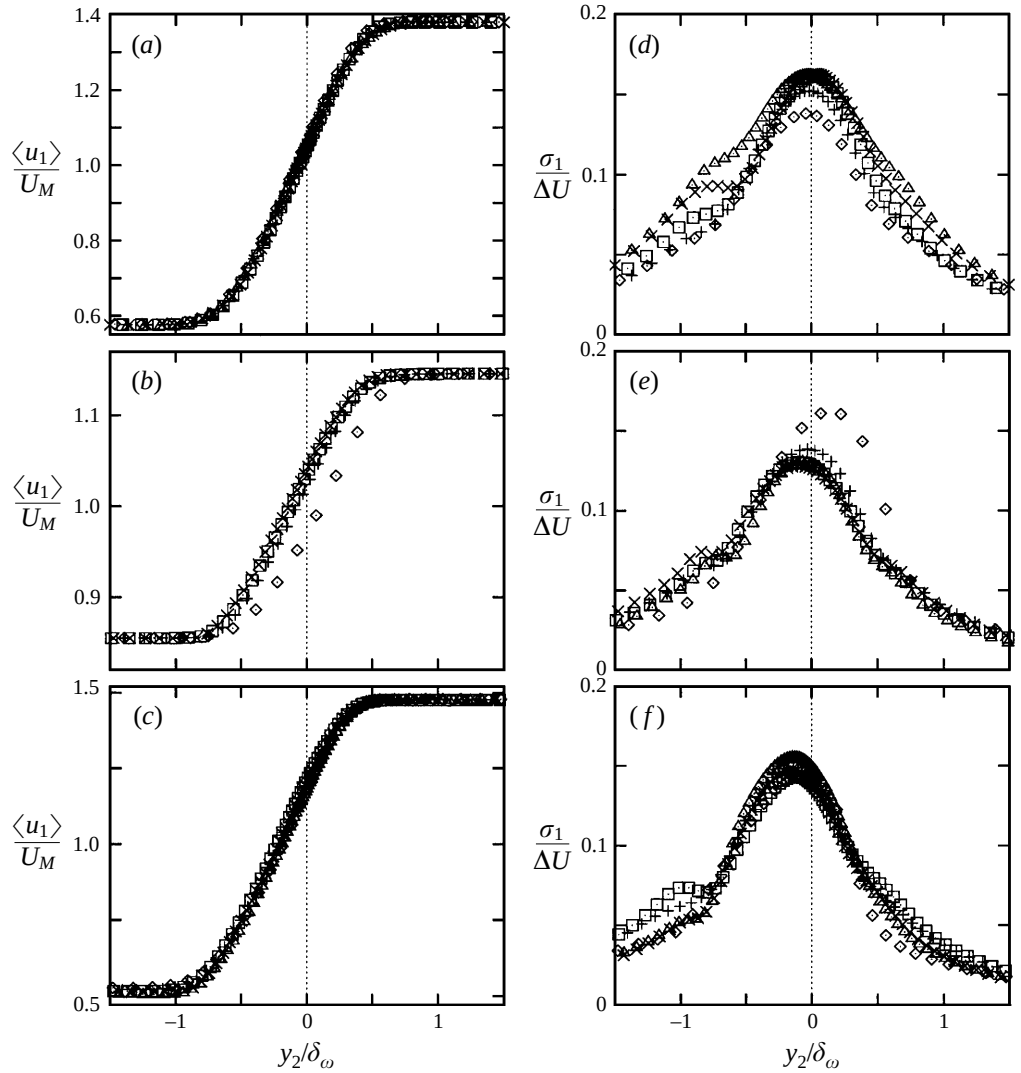

FIGURE 5. Similarity profiles. (*a–c*) Streamwise velocity; (*d–f*) streamwise turbulence. (*a*,*d*) case 1 ($M_c = 0.19$); (*b*,*e*) case 2 ($M_c = 0.33$); (*c*,*f*) case 3 ($M_c = 0.52$). ◇, $y_1/\delta_{\theta 0} = 1\,000$; +, $y_1/\delta_{\theta 0} = 2\,500$; □, $y_1/\delta_{\theta 0} = 4\,000$; ×, $y_1/\delta_{\theta 0} = 5\,500$; △, $y_1/\delta_{\theta 0} = 7\,000$.

supposed not to be correlated in time so that

$$\langle \tilde{u_1} u_1'' \rangle = 0.$$

This yields

$$\sigma_1 = (\tilde{\sigma}_1^2 + \sigma_1''^2)^{1/2}, \tag{2.2}$$

where

$$\tilde{\sigma_1} = (\langle \tilde{u}_1^2 \rangle - \langle \tilde{u}_1 \rangle^2)^{1/2},$$

$$\sigma_1'' = (\langle u_1''^2 \rangle)^{1/2}.$$

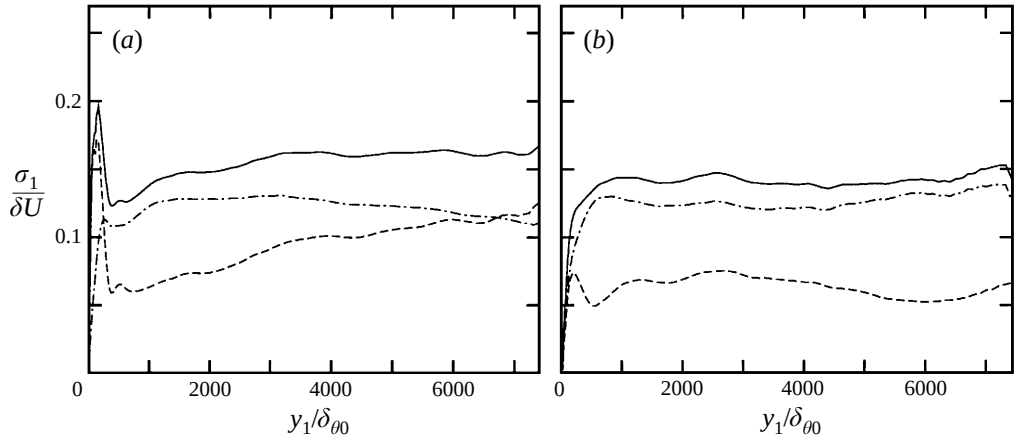

FIGURE 6. Streamwise evolution of the centreline r.m.s. velocity fluctuations in the shear layer. (*a*) case 1 ($M_c = 0.19$); (*b*) case 3 ($M_c = 0.52$). ——, total fluctuations $\sigma_1/\Delta U$; – – – –, coherent fluctuations $\tilde{\sigma}_1/\Delta U$;—·—, random fluctuations $\sigma_1''/\Delta U$.

The coherent r.m.s. fluctuation $\tilde{\sigma}_1$ is directly obtained from the calculation while the random part σ_1'' is deduced from the fine-grained turbulence model. Though it is not absolutely rigorous, let us assume that

$$\langle v_t \tilde{u}_1 \rangle \approx \langle v_t \rangle \langle \tilde{u}_1 \rangle,$$

where v_t is $\mu_t/\overline{\rho}$. One may then deduce from (2.1) that

$$\sigma_1''^2 = -\tfrac{2}{3}\langle v_t \rangle \left[2\frac{\partial \langle \tilde{u}_1 \rangle}{\partial y_1} - \frac{\partial \langle \tilde{u}_2 \rangle}{\partial y_2} \right] + \tfrac{2}{3}\langle k \rangle. \tag{2.3}$$

In the following the total r.m.s. velocity fluctuation σ_1 will be evaluated with (2.2) where the coherent r.m.s. fluctuation $\tilde{\sigma}_1$ is estimated from the time history of $\tilde{u}_1$ while the incoherent r.m.s. fluctuation σ_1'' is modelled with (2.3). It must be stressed that there are many approximations underlying (2.3), which must be considered with care. Yet, this seems the best way to take into account the contributions of both coherent and incoherent turbulence.

Thus, the similarity profiles of the total streamwise turbulence are plotted in figure 5 (*d*,*e*,*f*). In agreement with experimental observations, self-similarity is attained later and less clearly than for the mean flow profiles. The distance necessary is at least $4000\,\delta_{\theta 0}$ and it is hardly attained for case 1, for which we may invoke the fact that the 'development length' for turbulence quantities is longer for low convective Mach numbers (see e.g. Goebel & Dutton 1991). The peak value of σ_1 normalized by ΔU reaches a constant value for cases 1 and 2 of respectively 16% and 13% which is reasonable. For case 3, the normalized streamwise turbulence peak level may be compared favourably to the value of 17% indicated by Samimy & Elliott (1990). It may be noticed that some turbulence profiles show a lower secondary peak on the low-speed side. It is not known if this feature is important but it is indeed observed in some experimental profiles, e.g. measured by Barre, Quine & Dussauge (1994).

Now that the streamwise evolution of the total longitudinal turbulence has been illustrated, it is interesting to see more precisely how the two components $\tilde{\sigma}_1$ and σ_1'' behave independently. This may be observed in figure 6 (*a*,*b*) for cases 1 and 3. The situation is especially clear for the first case (figure 6*a*): if the transition zone that lasts

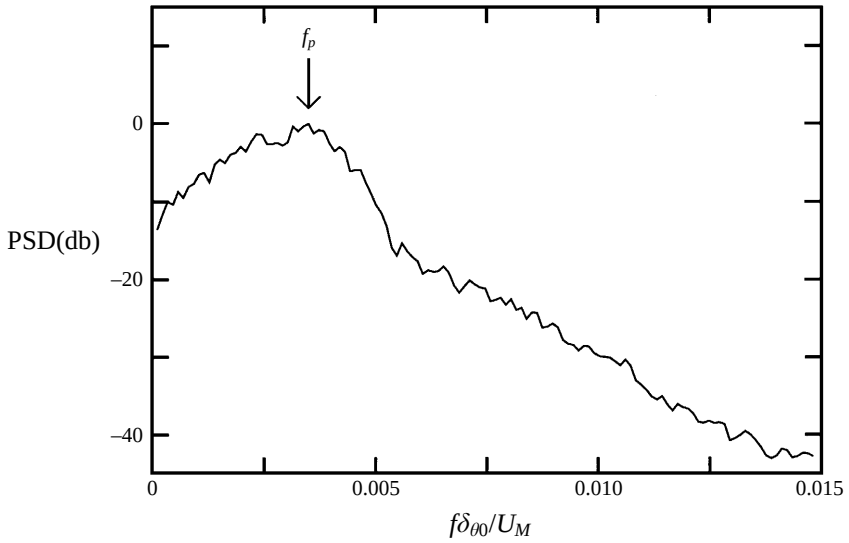

FIGURE 7. Estimation of the power spectral density of the centreline axial velocity fluctuations for the shear layer 1 at $y_1/\delta_{\theta 0} = 500$. The spectrum is plotted on an arbitrary decibel scale. The peak frequency is indicated by an arrow. The Fourier transform is performed on 15 segments of 512 points with a 50% overlap begore averaging. The spectral resolution is $\Delta f\, \delta_{\theta 0}/U_M = 5.6 \times 10^{-5}$.

about $1000\,\delta_{\theta 0}$ (a fact that can be deduced from figure 5*d*) is ignored, the coherent u_1 standard deviation $\tilde{\sigma_1}$ increases with respect to y_1 whereas σ_1'' slightly decreases so that the resulting total turbulence σ_1 is roughly constant. Thus, $\tilde{\sigma_1}$ profiles would not be self-similar and it is indeed essential to add the contribution of the modelled incoherent motion. Moreover, this opposite evolution of $\tilde{\sigma_1}$ and σ_1'' reflects an energy transfer between the coherent and fine-grained turbulence components. The energy coupling between $\tilde{u}_1$ and u_1'' is smaller for case 3 (figure 6*b*), but here again the total turbulence level obtained by adding coherent and stochastic contributions shows streamwise variations that do not exceed 5%.

2.2.4. *Spectral contents of the fluctuations*

The study of the similarity of the turbulence level only involves the standard deviation of the coherent motion velocity. The observation of the temporal spectrum of its fluctuations gives more insight into the coherent structures.

It is well known that the power spectral density of the velocity fluctuations measured in the middle of the shear layer peaks at a frequency f_p corresponding to the convection of the large-scale structures. Indeed a typical spectrum obtained from the computation of the first shear layer is shown in figure 7, where f_p can be clearly identified. The linear instability theory is a relevant method to get an estimate of the expected location of the spectrum peak. Thus the mean flow at a given streamwise location y_1 may be considered as a spatial amplifier for perturbations with appropriate frequency, and it has already been observed that the frequency $f_p^{(i)}$ corresponding to maximum spatial amplification rate provides a good prediction for f_p. For details on the application of the instability theory to convectively unstable flows the reader is referred to Huerre & Monkewitz (1990). Typically, the inviscid compressible theory

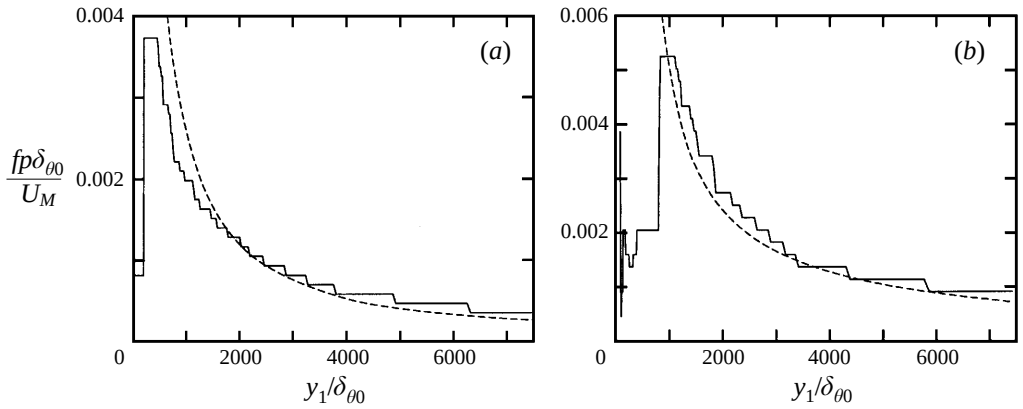

FIGURE 8. Centreline spectral development in the shear layer. (*a*) case 1 ($M_c = 0.19$); (*b*) case 2 ($M_c = 0.33$). ——, Peak frequency measured from numerical simulation; – – – –, prediction of the linear instability theory.

is here applied to a locally parallel shear flow and yields

$$f_p^{(i)} = St_0 \frac{U_M}{\delta_\omega},$$

where the value of the Strouhal number St_0 corresponds to a given mixing layer. The streamwise evolution of the frequency f_p determined from numerical spectra is shown in figure 8 for cases 1 and 2, together with the prediction $f_p^{(i)}$ from linear instability analysis. Apart again from the short zone ($y_1/\delta_{\theta 0} < 1\,000$) needed to establish the fully developed flow, the agreement observed is a strong indication that the coherent fluctuations of the flow are well captured by the computation.

2.3. *The C_μ parameter*

The influence of the C_μ parameter is now studied. The shear layers 1 and 3 have been calculated with $C_\mu = 0.05$ (instead of its traditional 0.09 value), all the other parameters being unchanged. There is no apparent modification of the coherent structure development. The mean flow grows linearly as in figure 3. The growth rate is slightly increased for the first shear layer: for example, the reduced Pitot growth rate δ''_{pit} changes from 0.87 to 0.93. There is almost no modification for case 3, where δ''_{pit} changes from 0.58 to 0.59. Thus, roughly speaking, the mean flow is unchanged, except perhaps that self-similarity is systematically reached further downstream than for $C_\mu = 0.09$. It is also possible to verify that the spectral development of the fluctuations is unchanged, meaning that the peak frequency of the aerodynamic spectra still evolves as shown in figure 8.

The principal modification concerns the energy balance between the computed coherent structures and the modelled stochastic motion. To show this, the streamwise evolution of the coherent, random and total fluctuation levels is plotted in figure 9 for the two shear layers 1 and 3. This must be compared to figure 6, showing the same evolution with the standard C_μ. Clearly, the incoherent motion level is a little lower with decreased C_μ while the coherent fluctuations level has increased. Owing to a different initial ratio of the coherent to incoherent motion in the two shear layers, the net effect on the total turbulence level is nearly zero for shear layer 3 while it is positive for shear layer 1, for which it increases from about 15% to 25%. This analysis is probably affected by the fact that full self-similarity is not attained for the

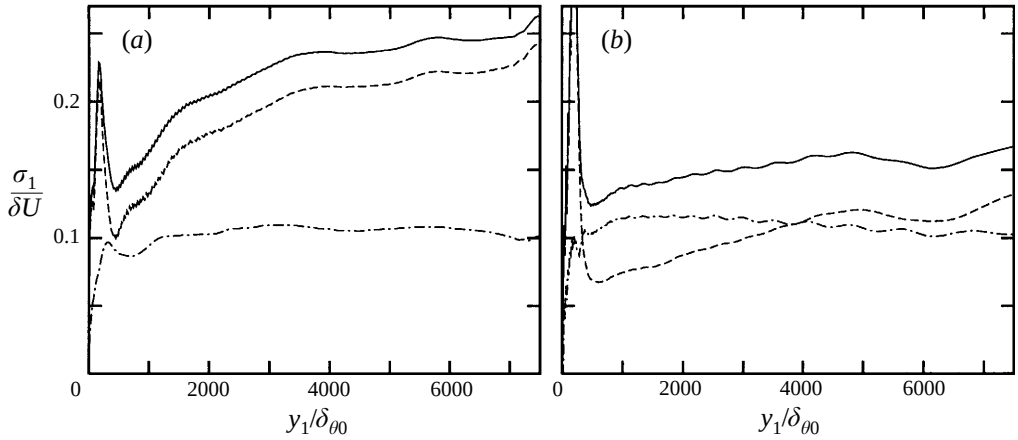

FIGURE 9. Streamwise evolution of the r.m.s. velocity fluctuations in the shear layer. Calculations with $C_\mu = 0.05$. Same conventions as in figure 6.

turbulent variables, so that turbulence levels have not yet reached their asymptotic values. Nevertheless, there is no doubt that the clearest effect of decreasing C_μ is to draw some energy from the incoherent motion (essentially modelled by the turbulent kinetic energy k) and to add some to the computed coherent fluctuations. Of course the details of the influence of a modification of C_μ may be a little more complicated but the procedure we adopt in the following is to use a value for which significant coherent motion can be observed, and then to compare the associated turbulence level to experimental data. It is shown in the next section that the amplitude of the coherent motion tends to be overestimated in jet flows, which in turn affects the evaluation of the radiated noise.

3. Plane jet flow computations

The two-dimensional mixing layer is a common test case for flow computations but is not suitable for noise calculations for several reasons. The source volume occupied by the turbulent flow is theoretically not limited in the streamwise direction which makes it difficult to evaluate the radiated noise, except by DNS. Besides, there is very little experimental data on shear layer noise and, in the absence of any other characteristic length scale, the results are highly dependent on the axial extent of the flow.

Thus, the jet case must be considered. In a first step, three-dimensional calculations are dismissed, so that the choice remains between the axisymmetric and the plane configuration. An axisymmetric jet featuring two-dimensional coherent structures (i.e. annular vortices) would be at first sight closer to reality than the plane jet. However such axisymmetric calculations would not capture helical large-scale instabilities which are known to be sometimes more efficient noise sources than axisymmetric ones. Moreover, both aerodynamic and acoustic computations are easier in the plane configuration. This is why this article deals with plane jet noise computations.

The present approach is not suitable for the prediction of shock-associated noise, for which specific models have to be developed, but only for mixing noise, so that only perfectly expanded jets are considered. For simplicity in the implementation of Lighthill's analogy and to begin with, the temperature ratio between the jet and the

M	Direction	Domain size	No. of points	Min. mesh spacing	Max. mesh spacing
0.50	y_1	25	142	0.08	0.32
	y_2	25	144	0.06	0.47
1.33	y_1	30	155	0.05	0.50
	y_2	20	156	0.04	0.36

TABLE 3. The plane jet computational grid. All dimensions are normalized by D.

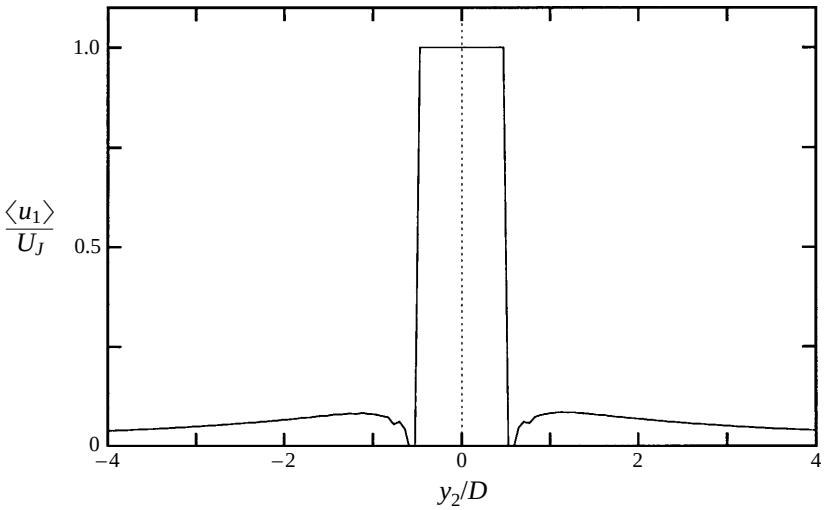

FIGURE 10. Mean inlet velocity profile for the subsonic jet ($M = 0.50$).

ambient fluid is kept constant and equal to 1 and only the exit Mach number is varied. Hence, two cold two-dimensional fully expanded jets have been calculated, at Mach numbers $M = 0.50$ and 1.33. The exit velocity is denoted U_J. The corresponding computational grids are described in table 3 where all dimensions are normalized by the nozzle height D. The nozzle itself is not included in the computational domain. Here again, y_1 and y_2 are the streamwise and transverse coordinates. The nozzle is centred on $y_2 = 0$.

Unless otherwise stated the calculations are performed in the same conditions as the shear layers. A notable exception is the inflow boundary conditions: all variables are imposed at the nozzle exit with a top-hat velocity profile, the nozzle lip is represented by one node with zero velocity, and the characteristics-based conditions that were already applied at the outflow are now used at the inflow outside the nozzle. To replace the incoming characteristics, the total pressure, total temperature and transverse velocity are imposed. A classical inlet velocity profile then naturally establishes as shown in figure 10 for the subsonic jet.

A more important difference with the shear layer must be indicated: if steady profiles are imposed at the nozzle exhaust, the coherent motion eventually vanishes. More precisely the structures are born in the two shear layers developing from the edges of the nozzle and grow normally as they are convected, but after the computational domain has been passed through two or three times by the flow the structure production suddenly stops. After the last structures have been convected out, the flow becomes nearly steady. This raises the fundamental problem of the

creation of the coherent structures. From an instability point of view, there must be some germ at the flow origin (we speak here of convectively unstable flows) and the perturbations are then amplified according to the theory. Experimentally, clean as the set-up may be, there is always some turbulence noise, especially in the boundary layers inside the nozzle, so that the starting of the structures is ensured, not to mention the case of a forced jet when the excitation is controlled. Numerically, the origin of the structures in the absence of excitation is not perfectly clear. Buell & Huerre (1988) suggest that some low-level numerical noise induced by spurious reflections at the outflow boundary condition may provide the necessary excitation. This explanation is reasonable but the study of the velocity spectra in §2 (see figure 8) shows that there is no strong phase locking of the coherent motion by such a mechanism. In other words, the structure production may be due to numerical noise but for our purpose it is random enough to mimic turbulence noise and natural shear layers (in contrast with excited shear layers).

With the hypothesis of Buell & Huerre (1988) in mind, it seems that the numerical noise level is not sufficient in the plane jet configuration. Thus, it becomes necessary to perturb the inlet profiles. The excitation must be designed with care so that it does not control the flow development. Besides, no spurious acoustic disturbances must be introduced in the flow. For this, let us consider the Euler equations linearized around the mean flow at the nozzle exit, i.e. with density $\rho_J + \delta\rho$, pressure $P + \delta p$, streamwise velocity $U_J + \delta u_1$ and transverse velocity δu_2. It is possible to show (see e.g. Giles 1990) that the disturbances which may propagate in the y_1-direction must be a linear combination of an entropy wave with phase speed U_J, a vorticity wave with phase speed U_J and two acoustic waves with phase speeds $U_J \pm c$, where c is the speed of sound. The Riemann invariants associated with each of these waves are respectively $\delta\rho - \delta p/c^2$, δu_2 and $\delta p \pm \rho_J c \delta u_1$. No acoustic wave should appear in the flow because of the excitation. For reasons given in §4, entropy variations must also be avoided. The excitation must then have

$$\delta\rho - \delta p/c^2 = 0,$$
$$\delta p \pm \rho_J c \delta u_1 = 0,$$

so that $\delta\rho = \delta p = \delta u_1 = 0$, which means that only the transverse velocity may be perturbed. The following profile is imposed:

$$\delta u_2 = \beta\, U_J\, \varepsilon(t)\, \Theta(y_2), \tag{3.1}$$

where β is a parameter that is kept at 0.005, $\varepsilon(t)$ is a zero-mean pseudo-random function with standard deviation 1 and $\Theta(y_2)$ a shape function peaking at 1 (see figure 11 *a*,*b*).

As shown experimentally, e.g. by Shih, Krothapalli & Gogieni (1992), the plane jet flow 'preferred mode', i.e. the frequency most likely to be amplified by the flow, corresponds to a Strouhal number St between 0.1 and 0.25 where $St = fD/U_J$. As the initial shear layers are certainly sensitive to higher frequencies, this band has been broadened on the high-frequency side and $\varepsilon(t)$ is constructed so that the corresponding spectrum $\varepsilon(f)$ is flat between $St = 0.2$ and $St = 0.5$ (see figure 11 *a*). To obtain a peudo-random function $\varepsilon(t)$, an inverse Fourier transform is performed from a finely discretized spectrum where all the components have been put randomly out of phase with each other. For the shape function, it has been observed that the preferred mode of a plane jet is generally antisymmetric (see Shih *et al.* 1992; Thomas & Goldschmidt 1986) and Θ has been chosen to feature this property and to be zero on the nozzle

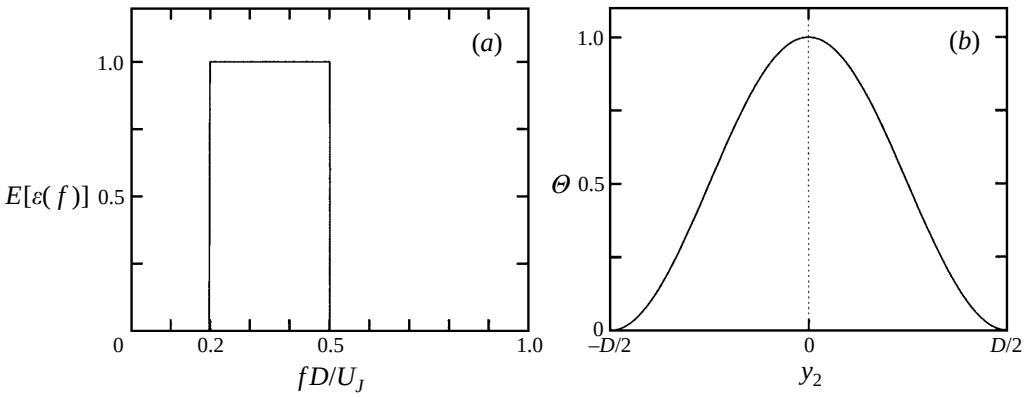

FIGURE 11. Nozzle inlet excitation used for the jet calculations $\delta u_2 = \beta\, U_J\, \varepsilon(t)\, \Theta(y_2)$. (*a*) Shape of the excitation spectrum $\varepsilon(f)$ with arbitrary vertical units. (*b*) Excitation spatial shape $\Theta(y_2)$.

walls for continuity:

$$\Theta(y_2) = \cos^2\left(\frac{y_2\pi}{D}\right) \text{ for } |y_2| \leqslant \tfrac{1}{2}D.$$

The maximum amplitude of the excitation function, here 0.5% of the exit velocity, should not be an important parameter provided it is low enough. This will be verified in the following. We mean that the intensity of the fluctuations induced by the excitation is expected to be determined by nonlinear saturation phenomena and not to be scaled by the excitation itself.

After a set of preliminary tests it was found that it was much easier to maintain coherent perturbations with low excitation levels when the constant C_μ was reduced, in agreement with Ha Minh's (1994) observations. Consequently, the plane jets were computed with $C_\mu = 0.05$.

Snapshots of the two flows are displayed in figure 12 in the form of passive scalar contours. The evolution with increasing Mach number is quite clear. In the subsonic jet, the two shear layers developing from the edges of the nozzle grow rapidly and show large and distinct coherent structures. Correspondingly, the potential region of the jet seems short. The situation is different for the supersonic jet, developing more slowly and where the large structures look more like an oscillation of the jet column. Before quantifying these observations, let us mention that the general aspect of coherent structures when M is varied is in agreement with experimental findings: consider e.g. the spectacular vortex rings in a low-speed jet in Longmire & Eaton (1994) in contrast with the wave-like coherent fluctuations shown by Lepicovsky *et al.* (1985) for a jet at Mach number 1.37, in both cases with circular nozzle.

The potential core extension with increasing Mach number is confirmed in figure 13, where the centreline velocity profile is plotted for the two jets, along with an experimental profile from Kouts & Yu (1974) for a rectangular jet at $M = 0.50$ with a nozzle aspect ratio $\mathscr{A} = 10$. The collapse of numerical and experimental results for the subsonic jet should not be given a meaning that it has not. The numerical curve was obtained from a two-dimensional plane calculation while the experimental flow is a rectangular jet with an aspect ratio that is not so high that three-dimensional effects may be completely neglected. Thus, one should not conclude that reality is perfectly described by the computation. However, this proves that quite reasonable aerodynamic results may be obtained with SDM on realistic spatially evolving jet flows, which to the best of our knowledge has not yet been observed with LES.

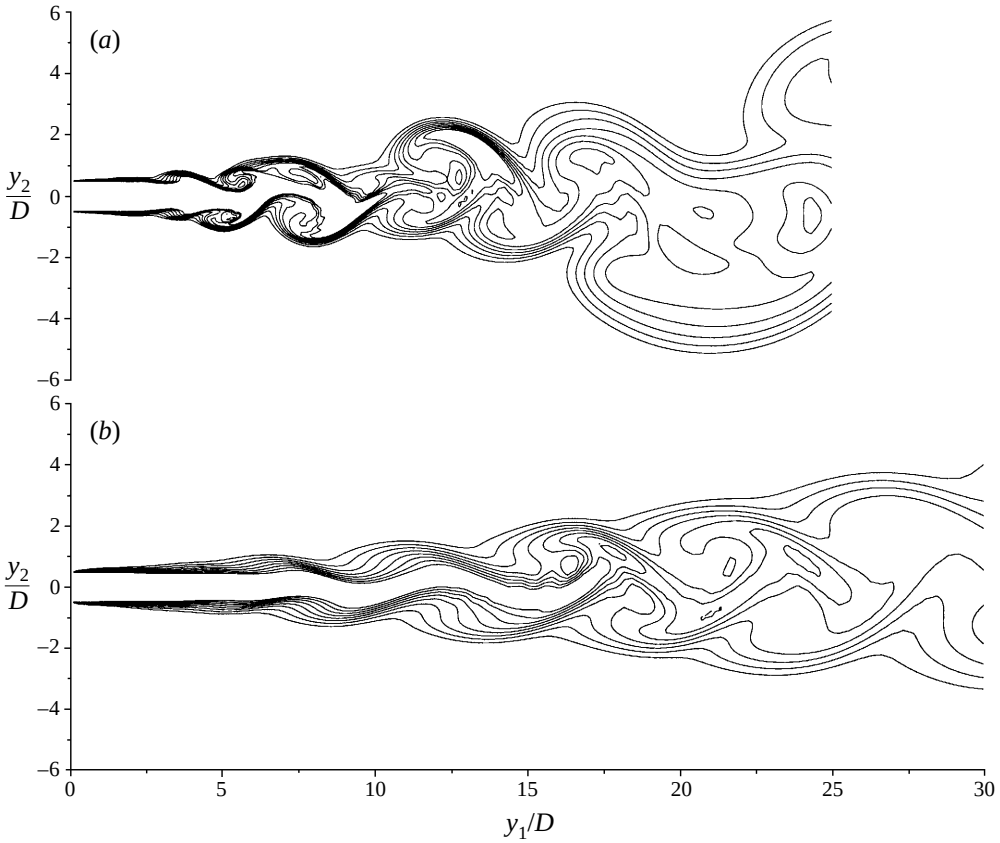

FIGURE 12. Instantaneous passive scalar field in the plane jet flows. (*a*) $M = 0.50$; (*b*) $M = 1.33$. Same conventions as in figure 3.

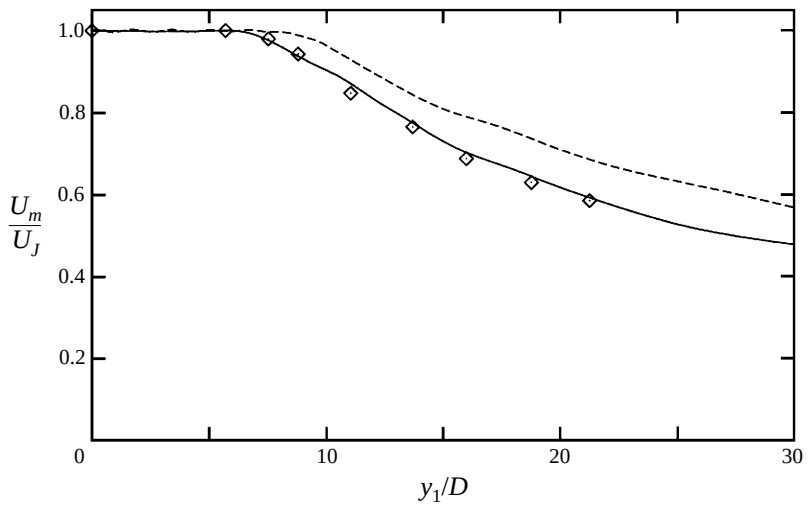

FIGURE 13. Development of mean longitudinal velocity on jet centreline: ——, $M = 0.50$; – – – –, $M = 1.33$; ◇ measurements by Kouts & Yu (1974) for $M = 0.50$.

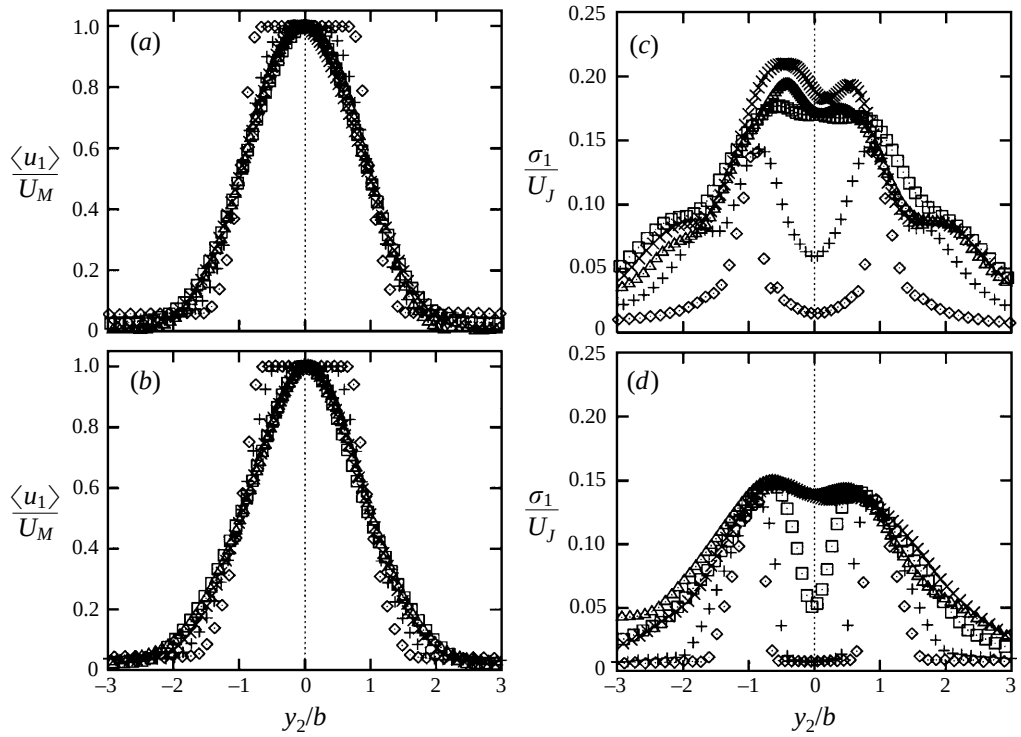

FIGURE 14. The jets mean flow development. (*a*,*b*) Transverse profiles of streamwise velocity; (*c*,*d*) transverse profiles of streamwise turbulence. (*a*,*c*) $M = 0.50$; (*b*,*d*) $M = 1.33$. ◇, $y_1/D = 2.5$; +, $y_1/D = 5$; □, $y_1/D = 10$; ×, $y_1/D = 20$; △, $y_1/D = 25$.

For the supersonic jet, we are not aware of any relevant experimental data but the evolution from the subsonic jet is similar to what can be observed for circular jets. More generally, there seem to be very few aerodynamic experimental results for high-aspect-ratio rectangular jets, other than very low-speed ones ($M \leqslant 0.2$). This is why in the remainder of §3 no further comparison of numerical and experimental plots can be provided, though a discussion of the results remains possible.

The transverse profiles of streamwise velocity at different x-locations plotted in figure 14(*a*,*b*) show that the two jets are fully developed at $y_1 = 20D$. The profile obtained when self-similarity is attained may be very well approximated by a Bickley quasi-Gaussian profile. The total streamwise turbulence profiles plotted in figure 14(*c*,*d*) were obtained as in §2 as the sum of the calculated coherent r.m.s. fluctuation and the incoherent turbulence modelled by (2.3). In contrast with the velocity profiles, self-similarity is not attained yet. The axial location where the two shear layer turbulence peaks merge is directly correlated with the end of the potential core and increases with the Mach number.

The centreline distribution of the total streamwise turbulence intensity is more precisely seen in figure 15(*a*). The maximum level attained is 18% of the exit velocity in the subsonic jet and 15% in the supersonic jet. These values may be compared to measurements performed by Lau, Morris & Fisher (1979) on circular jets. A value of about 15% is typically obtained at Mach numbers 0.28 and 0.90 and 13.5% at Mach number 1.37. Thus, the computed levels are quite reasonable, maybe a

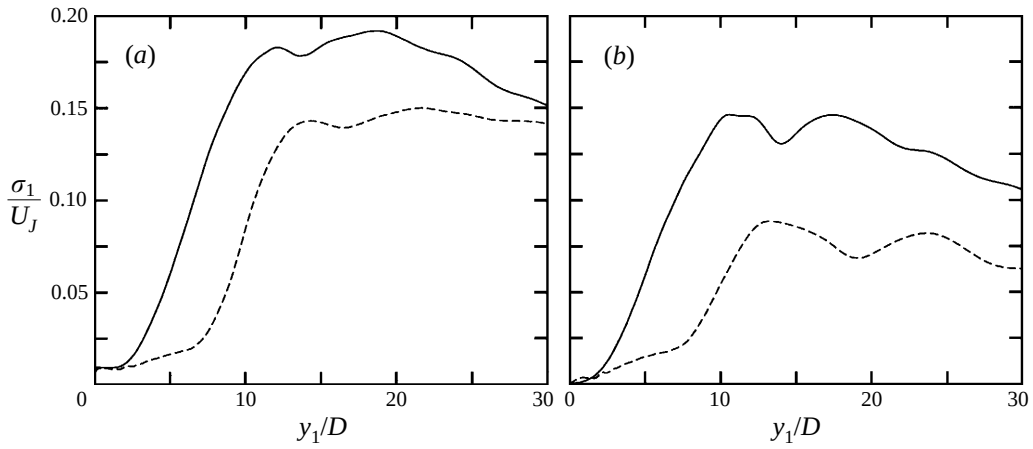

FIGURE 15. Streamwise evolution of the centreline r.m.s. velocity fluctuations in the plane jets. (*a*) Total fluctuations σ_1/U_J; (*b*) coherent fluctuations $\tilde{\sigma_1}/U_J$. ——, $M = 0.50$; – – – –, $M = 1.33$.

little overestimated for the subsonic jet. But what is more our concern here is the coherent turbulence level, that is the level of the computed coherent fluctuations. Figure 15(*b*) displays the streamwise coherent turbulence level along the centreline. It appears that the maxima reached for the two jets are respectively 15% and 9%. Owing to the definition of the coherent structures concept, it is difficult to practically assess the fraction of the total turbulent energy represented by the coherent motion. Nevertheless, some authors have attempted to give an estimate of this ratio in jets, e.g. Mumford (1982) obtained 20% in a low subsonic rectangular jet and Lepicovsky *et al.* (1985) observed values of 10% to 20% in a circular jet at Mach number 1.37. Therefore, considering the data of Lau *et al.* cited above, we should expect to observe coherent turbulence levels no higher than 3%. Of course, it is a crude estimate but it means that the intensity of the computed aerodynamic fluctuations is almost certainly too high, especially for the subsonic jet. From what has been observed in the shear layer study, we know that a weaker coherent motion may be obtained by increasing the turbulence model constant C_μ. However a parametric study with respect to the value of C_μ would be a difficult task with limited interest. It is not our purpose to proceed to a complete recalibration of the model in free shear flows, which would indeed provide the solid basis from which the choice of the C_μ constant could be established. Thus, at this stage, the aerodynamic calculation is kept as it is. Whereas the space–time characteristics of the coherent structures are realistic, their intensity is probably too high. This uncertainty on the coherent motion level should be borne in mind when considering the acoustic results in §5, in the sense that it correspondingly affects the absolute level of the computed radiated noise.

As for the shear layer case, the spectral contents of the coherent fluctuations evolves along the flow. To verify this, the spectra of $\tilde{u_1}$ measured in the middle of the shear layer (or more precisely one of the two shear layers) is shown in figure 16 (*a*,*b*) for each jet at different axial locations. As may be expected from simple dimensional arguments, the spectral densities shift towards lower frequencies as the flow develops. In fact, various experiments (see e.g. Thomas & Goldschmidt 1986) have shown that in low-speed plane jets the peak frequency of the cross-spectral density

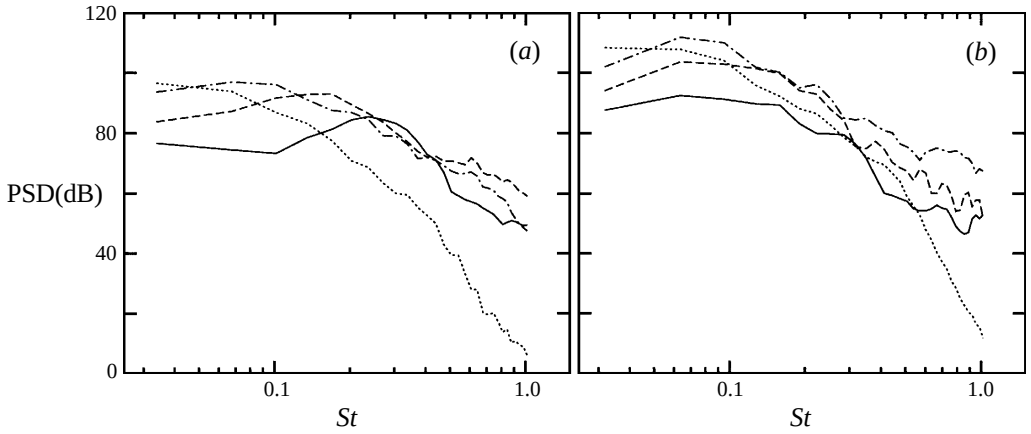

FIGURE 16. Power spectral density of the jet axial velocity fluctuations in a shear layer ($y_2/D = 0.5$), with arbitrary reference level (0 dB). (*a*) $M = 0.50$; (*b*) $M = 1.33$. ——, $y_1/D = 2$; – – –, $y_1/D = 5$; —·—, $y_1/D = 10$; ·····, $y_1/D = 20$.

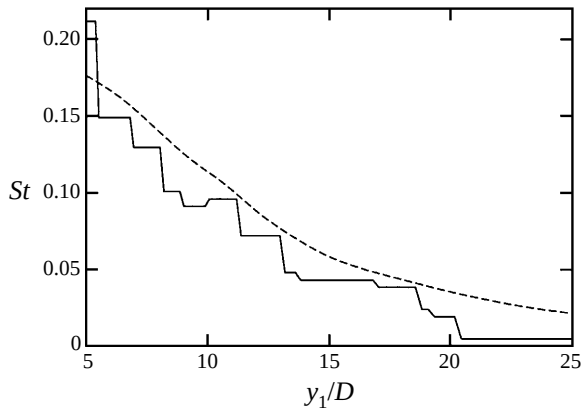

FIGURE 17. Centreline spectral development in the subsonic jet. ——, Peak frequency f_p measured from numerical simulation; – – –, empirical law $f = 0.11\, U_m/b$. Only the fully developed region of the jet, starting about $y_1 = 5\,D$, is represented.

between streamwise velocities in the jet shear layers evolves according to

$$f_c = 0.11\,\frac{U_m}{b}, \tag{3.2}$$

where U_m is the mean centreline velocity and b the velocity profile half-width. In the fully developed region of the jet, where the two shear layers can no longer be distinguished anymore, f_c is identical to the centreline velocity peak frequency f_p, as defined in figure 7. The empirical law (3.2) evaluated from the computed mean flow and the peak frequency of the centreline velocity fluctuations spectra are compared in figure 17 for the subsonic jet.

Two observations can be made from this plot. First, the frequencies of the computed coherent structures are in accord with the evolution deduced from the spatial development of the jets. Second and more important, the peak frequency f_p is not a perfectly smooth function of the axial location. This discontinuous behaviour is more pronounced than in the single shear layer case (compare to figure 8). This

is partly due to a reduced spectral resolution but it also indicates that the spectra measured in the jet present a slight discrete character, suggesting that a finite number of jet instability modes have been excited. Of course, this number is sufficiently important that the spectra shown in figure 16 contain no distinct peaks, which would be the signs of a tone-excited jet. Nevertheless, it proves that it was necessary to verify the spectral contents of the fluctuations before asserting that a reasonable natural jet had been computed. In fact we previously checked that when the inflow excitation is too tightly centred near a preferred frequency of the flow, the jet becomes nearly periodic and the coherent structure development is replaced by a global perturbation of the flow, where the spectra measured at different spatial locations all show the same strong peaks. This configuration, more representative of a tone-excited jet, leads to very poor acoustic results and is of little interest for our present purpose.

4. Numerical implementation of Lighthill's analogy

In what follows, the sound field is evaluated from Lighthill's analogy. One restriction of this framework is that it cannot account for refraction effects. Now these effects mainly influence high-frequency radiation and are of lesser importance for the sound emission of large-scale turbulence components. Nevertheless we here favour Lighthill's approach because it is the most tractable numerically. It is also shown that its formulation in conjugate space yields a physically appealing interpretation.

4.1. *Three possible formulations*

In its basic form, the analogy derived by Lighthill in 1952 from the conservation equations of motion states that

$$\left(\frac{\partial^2}{\partial t^2} - c_0^2 \frac{\partial^2}{\partial y_i \partial y_i}\right)(\rho - \rho_0) = \frac{\partial^2 T_{ij}}{\partial y_i \partial y_j}, \tag{4.1}$$

where the subscript 0 denotes quantities at rest and T_{ij} is Lighthill's tensor:

$$T_{ij} = \rho u_i u_j + [(P - P_0) - c_0^2(\rho - \rho_0)]\delta_{ij} - \tau_{ij}. \tag{4.2}$$

In this expression, δ_{ij} is the Kronecker symbol and τ_{ij} the viscous stress tensor. It should be noted that (4.1) is an exact reformulation of Navier–Stokes equations.

In most practical situations, it may be assumed that the source term is non-zero only in a region of finite extent. Then, for any observation point $\boldsymbol{x}$ exterior to this source volume $\mathscr{V}$, the application of the Green's function formalism yields

$$\rho(\boldsymbol{x}, t) - \rho_0 = \frac{1}{4\pi c_0^2} \int_{\mathscr{V}} \frac{1}{|\boldsymbol{x} - \boldsymbol{y}|} \frac{\partial^2 T_{ij}}{\partial y_i \partial y_j} \left(\boldsymbol{y}, t - \frac{|\boldsymbol{x} - \boldsymbol{y}|}{c_0}\right) \mathrm{d}\boldsymbol{y}. \tag{4.3}$$

This expression gives the density fluctuations in the region where it is assumed that the source term, containing the density and speed fluctuations, is zero. The tacit assumption here is that the fluctuations outside $\mathscr{V}$, of acoustic nature, are negligible compared to the turbulent fluctuations existing in the source volume so that a separation may be established between the two regions. The only true limitation of Lighthill's analogy is here: phenomena for which no such distinction is possible cannot be taken into account, two important examples being the refraction of sound by the mean flow and shock-associated noise. It is, on the other hand, well adapted to the prediction of jet mixing noise.

In the far-field approximation, (4.3) becomes

$$\text{formulation (1)} \qquad \rho_a(\boldsymbol{x},t) = \frac{1}{4\pi c_0^2 x}\int_{\mathscr{V}} \frac{\partial^2 T_{ij}}{\partial y_i \partial y_j}\left(\boldsymbol{y}, t - \frac{|\boldsymbol{x}-\boldsymbol{y}|}{c_0}\right) \mathrm{d}\boldsymbol{y}, \tag{4.4}$$

where ρ_a designates the acoustic density perturbations and with $x = |\boldsymbol{x}|$. In the following, we will refer to (4.4) as the first formulation of Lighthill's analogy. Another formulation may be derived by applying the divergence theorem twice (see e.g. Blake 1986). One obtains

$$\begin{aligned}\rho_a(\boldsymbol{x},t) = {} & \frac{1}{4\pi c_0^2 x}\int_{\mathscr{S}} \frac{\partial T_{ij}}{\partial y_j}\left(\boldsymbol{y}, t - \frac{|\boldsymbol{x}-\boldsymbol{y}|}{c_0}\right) \mathrm{d}S_i(\boldsymbol{y}) \\ & + \frac{1}{4\pi c_0^2 x}\frac{\partial}{\partial x_i}\int_{\mathscr{S}} T_{ij}\left(\boldsymbol{y}, t - \frac{|\boldsymbol{x}-\boldsymbol{y}|}{c_0}\right) \mathrm{d}S_j(\boldsymbol{y}) \\ & + \frac{1}{4\pi c_0^2 x}\frac{\partial^2}{\partial x_i \partial x_j}\int_{\mathscr{V}} T_{ij}\left(\boldsymbol{y}, t - \frac{|\boldsymbol{x}-\boldsymbol{y}|}{c_0}\right) \mathrm{d}\boldsymbol{y}, \end{aligned} \tag{4.5}$$

where $\mathscr{S}$ is the surface delimiting $\mathscr{V}$. As $\mathscr{V}$ is supposed to enclose the source region, the surface integrals are zero and after developing the derivations with respect to $\boldsymbol{x}$ the second formulation reads

$$\text{formulation (2)} \qquad \rho_a(\boldsymbol{x},t) = \frac{1}{4\pi c_0^4 x}\int_{\mathscr{V}} \frac{\partial^2 T_{rr}}{\partial t^2}\left(\boldsymbol{y}, t - \frac{|\boldsymbol{x}-\boldsymbol{y}|}{c_0}\right) \mathrm{d}\boldsymbol{y},$$

where T_{rr} is the component of T_{ij} in the observer direction:

$$T_{rr} = \frac{x_i x_j}{x^2} T_{ij}.$$

Finally, the third formulation is obtained by taking the Fourier transform in time of the previous one and applying the far-field approximation:

$$\text{formulation (3)} \qquad \rho_a(\boldsymbol{x},\omega) = -\frac{\exp(\mathrm{i}\omega x/c_0)}{4\pi c_0^4 x}\,\omega^2\, T_{rr}\left(\boldsymbol{\kappa} = \frac{\omega}{c_0}\frac{\boldsymbol{x}}{x}, \omega\right),$$

where the space and time Fourier transforms are defined by

$$g(\boldsymbol{\kappa},\omega) = \int g(\boldsymbol{y},t)\,\exp[-\mathrm{i}(\boldsymbol{\kappa}\cdot\boldsymbol{y} - \omega t)]\,\mathrm{d}\boldsymbol{y}\,\mathrm{d}t.$$

The same notation is used for the function and its transform, the arguments employed removing any ambiguity.

The previous expressions yield different theoretical interpretations. Formulations (1) and (2) indicate that the sound produced at the observation point $\boldsymbol{x}$ at time t is given by the contributions of the source term at retarded time. In the limit of low-Mach-number flows, the source term is compact and the effect of the variation of retarded time within the source volume is nearly negligible, except for the fact that it prevents the complete cancellation of the integral in formulation (1). Thus, valuable predictions concerning low-speed jet noise have been obtained analytically from these formulations by Lighthill (1952), the most famous one being probably the dimensional law accounting for the growth of the radiated acoustic power with the eighth power of the exit velocity.

Ffowcs Williams showed in 1963 that formulation (3) leads to a simple explanation of the evolution of jet noise over a wide range of Mach numbers. We will show in this paper that the analysis of this formulation, which is also evoked by Crighton (1975),

provides an illuminating interpretation of the corresponding acoustic computations. For this, let us consider the sound emitted in the plane $(y_1 y_2)$, i.e. with no azimuthal angle, in the direction making an angle θ with the jet downstream direction (the y_1-axis). On one hand, formulation (3) shows that the space–time Fourier components of the source term T_{rr} that contribute to the radiated noise are those for which $\boldsymbol{\kappa}$ points towards the observer and such that

$$\omega = \kappa c_0, \tag{4.6}$$

where $\boldsymbol{\kappa} = \kappa \boldsymbol{x}/x$. On the other hand, the distribution of T_{rr} in the conjugate (κ, ω)-space is strongly influenced by the convection effect of the mean flow. Thus, in a jet, the aerodynamic fluctuations are known to be essentially convected at speed U_c parallel to the mean flow. In fact, U_c may be interpreted as the convection speed of the large-scale structures, on which is superimposed the fine-scale turbulent motion. Of course, this is a simplified representation of the turbulence in a jet flow and from another point of view, this convection speed is the group velocity of the instabilities supported by the mean flow and must be local and frequency-dependent. Nevertheless, the frequently used assumption of constant U_c in free shear flows is known to be reasonable. In the wavenumber–frequency space, this means that the source term in Lighthill's analogy will attain its maximum when

$$\omega = \boldsymbol{\kappa} \cdot \boldsymbol{U}_c,$$

which becomes, when $\boldsymbol{\kappa}$ is aligned with the observer direction $\boldsymbol{x}$,

$$\omega = \kappa U_c \cos\theta. \tag{4.7}$$

Interesting features of jet mixing noise can be understood by considering the relative position of the *sonic line* defined by (4.6) of the spectral components that effectively radiate and the *convection line* given by (4.7) around which the source term is localized. The basis of this interpretation is illustrated in figure 18 (*a*,*b*).

The situation where the convective Mach number $M_c = U_c/c_0$ is less than 1 is shown in figure 18(*a*). For a 0° observation angle, i.e. when the observer is downstream on the jet axis, the slope of the convection line is lower than that of the sonic line. Only a small part of the dominant source term components contribute to the radiated noise. When the observation angle increases, the convection line slope is reduced and the contribution of the source term to the sound field is even lower. The directivity should then be maximum for $\theta = 0°$ and slowly decreasing with θ.

On the other hand, if the convection speed is supersonic ($M_c > 1$) (see figure 18*b*), when $\theta = 0°$ the slope of the convection line is higher than that of the sonic line. As θ increases, the two lines come closer to each other and most of the coherent fluctuations contribute to the radiated noise. The lines are superposed for θ_0, verifying

$$\cos\theta_0 = \frac{1}{M_c}, \tag{4.8}$$

and the convection line moves away again for $\theta > \theta_0$. In this case the sound directivity may be expected to be strongly peaked around the angle θ_0, determined by (4.8). For this particular angle, the structure convection speed seen by the observer, i.e. projected on the observation direction, is precisely the speed of sound c_0. The strong radiation corresponding to this case is thus a Mach wave radiation and θ_0 is the Mach wave angle.

The ratio of the convection velocity to the jet exit speed is usually estimated at two thirds for a circular jet. Then, for a cold jet the transition between the two

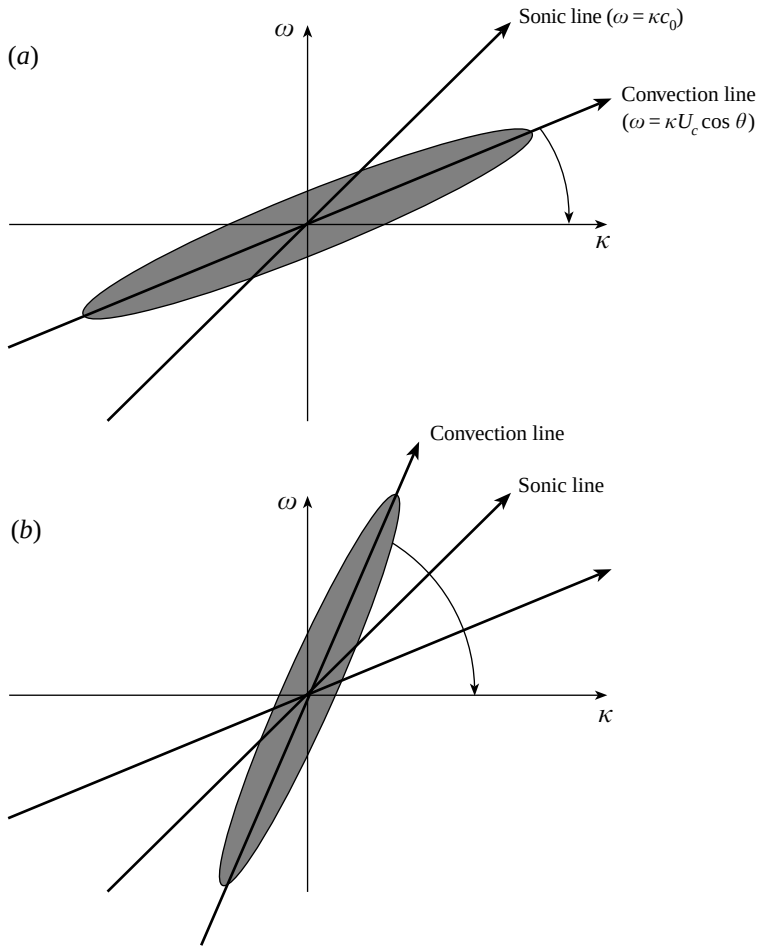

FIGURE 18. Interpretation of Lighthill's analogy in (κ, ω)-space. (a) Situation where $U_c < c_0$; (b) situation where $U_c > c_0$. The convection line is plotted for an observation angle $\theta = 0$ and the curved arrow indicates its evolution when θ increases. The shaded area represents the expected localization of the source term along the convection line.

situations just described should occur for $M \simeq 1.5$, which make the two computed jets representative of the first case ($M_c < 1$). However, following this interpretation, the supersonic jet should feature a directivity much more strongly peaked at $\theta = 0^\circ$ than the subsonic jet, as will be verified in §5.

The qualitative prediction of the directivity changes with the jet Mach number, directly derived from the analysis of formulation (3), is in agreement with experimental data on fully expanded jet noise. An exception is the directivity drop-off at small observation angles due to refraction, which cannot be captured via Lighthill's approach. More generally, the formulation of Lighthill's analogy expressed in (κ, ω)-space provides a geometrical interpretation which, as shown in §5 proves extremely useful for understanding acoustic computations. The computed directivity and the radiation spectra may be analysed in connection with the space–time spectral distribution of the source term.

4.2. *The choice of a formulation*

The three formulations of Lighthill's analogy given previously are based on the same source term T_{ij}. This quantity is the sum of three terms as may be seen from (4.2): the Reynolds stress tensor $\rho u_i u_j$, a term describing the deviation from isentropy and the opposite of the viscous stress tensor. For high-Reynolds-number flows it is well-known that the third term is negligible compared to the first one. The second term should in principle be retained. However, in the particular case where the temperature in the jet is equal to the ambient temperature, the local speed of sound may be expected to show little variations from c_0. Besides, the heat dissipation effects are of the same magnitude as the viscous effects and can be neglected, so that in the absence of any shocks, i.e. for a fully expanded jet, the flow may be considered isentropic and the second term can also be neglected. Yet, this approximation is not fundamental: here we use it in a first step to simplify the calculations but this it is not essential and the present approach could be extended to treat hot jets. Under these conditions, one has

$$T_{ij} \simeq \rho u_i u_j.$$

It is worth noting that the formulations introduced in §4.1 are explicit though the variable ρ appears on both sides of these equations, and this because the observation point $\boldsymbol{x}$ is outside the integration volume. Thus, there is no need to replace ρ by ρ_0 in the expression for T_{ij} and the source term does contain the fluctuating density as well as the fluctuating turbulent velocity.

In the aerodynamic computations described in §3, the three variables ρ, u_1 and u_2 are stored with a time increment between two storages of $0.50\,D/U_J$, so that the maximum frequency that can be explored corresponds to $St = 1$. Because of the assumption of two-dimensional coherent motion, the spanwise velocity component u_3 is zero. The data storage begins only when the flow may be assumed fully developed, that is after the computational domain has been passed through at least once. 1024 time steps are recorded, which is the result of a compromise between the desired spectral resolution and storage capacity considerations.

In formulation (1), the source term is the double divergence of Lighthill's tensor. The tensor is symmetric and three non-zero components must be evaluated. The spatial derivatives are estimated with second-order finite difference approximation on a nine-point stencil. If the evolution of the mesh size in each direction is slow, the truncation error depends quadratically of the spatial grid step. Note that for a realistic flow field such as the jet flow, the source term is not spatially periodic, and it is not suitable to evaluate the spatial derivatives in the Fourier-transformed space. To obtain the sound field at time t, the source term must be evaluated at retarded time $t - |\boldsymbol{x} - \boldsymbol{y}|/c_0$. To be consistent with the derivation of formulation (3), this retarded time is evaluated in the Fraunhofer approximation:

$$t - \frac{|\boldsymbol{x} - \boldsymbol{y}|}{c_0} \simeq t - \frac{x}{c_0} + \frac{\boldsymbol{x} \cdot \boldsymbol{y}}{c_0 x}. \tag{4.9}$$

However, the source term is available only on a discrete space–time grid. As is shown by Sarkar & Hussaini (1993), it is dangerous to simply replace the true retarded time by the closest time for which the source term is available. Therefore, it is necessary to proceed to a spatial or temporal interpolation. It is much simpler to use a temporal interpolation so that, for each grid point $\boldsymbol{y}$, the source term at retarded time is estimated by linear interpolation in time.

The trapezoidal rule is used for spatial integration. It is easily shown that the time average of the source term does not radiate. Indeed:

$$\int_{\mathscr{V}} \frac{\partial^2 \langle T_{ij} \rangle}{\partial y_i \partial y_j}(\boldsymbol{y})\,\mathrm{d}\boldsymbol{y} = 0,$$

and thus only the fluctuations of the source term need to be retained. Besides, some precautions have to be taken so that truncation effects would not strongly influence the computed acoustic field. This is achieved by tapering the fluctuations of $\partial_{ij} T_{ij}$ on the edges of the source volume by a decreasing Gaussian.

The radiated sound field may then be calculated when the source term is known at retarded time all over the computational domain, that is during a time interval slightly shorter than the time interval during which the source term was stored. It is straightforward to see that the difference between these two intervals is roughly the retarded time lag between the two most distant points in the source volume, that is about L/c_0 where L is the source volume length (and largest dimension). Thus, the radiated noise is calculated for 1024 evenly spaced times with a time step slightly lower than the initial storage step. The spectral analysis of this signal is then obtained by averaging 15 segments of 128 points with a 50% overlap. A temporal Hann square-sine window, which presents a high sidelobe decay rate, is applied to each segment.

Computations with formulation (2) are quite similar to those described above, except that temporal second derivatives of T_{ij} have to be evaluated instead of spatial derivatives. This term is estimated through a second-order centred finite difference approximation:

$$\frac{\partial T_{ij}}{\partial t^2}(t) = \frac{T_{ij}(t-\Delta t) - 2T_{ij}(t) + T_{ij}(t+\Delta t)}{\Delta t^2} + O(\Delta t^2). \tag{4.10}$$

Formulation (3) expressed in the Fourier-transformed space requires different processing. The space–time spectral contents of Lighthill's tensor has to be evaluated on the sonic line, determined by (4.6). Because wavenumber and frequency are not independent, it is not helpful to use a fast Fourier transform algorithm and the space–time Fourier integral is calculated directly via the trapezoidal rule. As for the first two formulations, the source term is modulated on the edges of the source volume and the integral is performed on 15 overlapping time segments of 128 points each on which the spectral density is averaged.

Before discussing the results obtained with each of the three formulations, a few precautions taken to scale the acoustic data should be mentioned. The three formulations involve a spatial integration over the source volume. In the computations, what is available is a two-dimensional source surface and some modelling of the structure in the third dimension (y_3) must be introduced to allow comparisons with three-dimensional rectangular jet noise data. Let us consider a rectangular jet with nozzle dimensions D and $\mathscr{A}D$, where $\mathscr{A}$ is the nozzle aspect ratio. The plane jet computation is supposed to represent the development of this real jet in the (y_1, y_2)-plane containing the nozzle dimension D. This is reasonable only if $\mathscr{A}$ is high enough (say more than 10), for then rectangular jets may exhibit two-dimensional large-scale coherent structures. Now, for simplicity, the point of observation $\boldsymbol{x}$ will be kept in the (y_1, y_2)-plane (see figure 19). In other words, only the radiation of the jet at zero azimuthal angle is considered. The observation point is then completely determined by knowing the observation distance x and the polar angle θ. Consequently, as may be seen from (4.9), all points located on a line parallel to the y_3-direction emit in

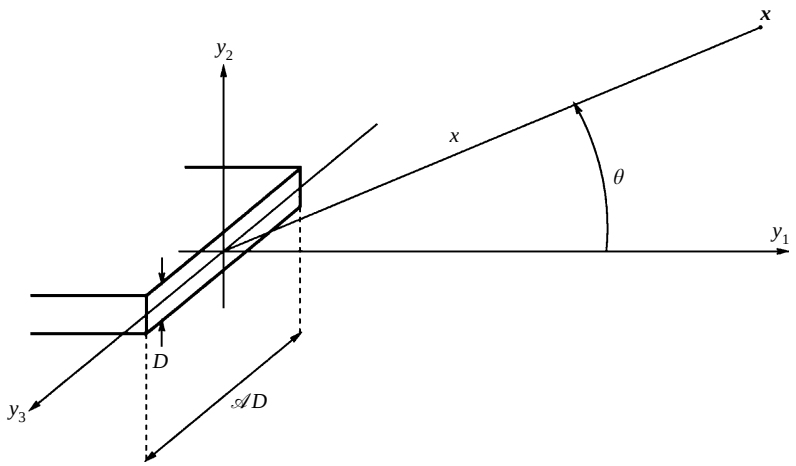

FIGURE 19. Definition of nozzle geometry and acoustic observation point coordinates.

phase, and at first sight the y_3 integration of the source term introduces a factor $\mathscr{A}D$. The acoustic intensity would then scale with $\mathscr{A}^2$, though it is known to scale with the nozzle exit surface, i.e. with $\mathscr{A}$. The paradox is removed if we consider that it is not realistic to assume that the coherent fluctuations are completely correlated in the y_3-direction. Thus, it is necessary to introduce a correlation width Λ of the fluctuations. Considering the approximation level of a rectangular jet by a plane jet, it does not seem relevant to set a complicated expression for Λ and we will assume that Λ is simply proportional to D with a factor α:

$$\Lambda = \alpha D. \tag{4.11}$$

The rectangular jet of spanwise extent $\mathscr{A}D$ may then be decomposed into elementary jets of width 2Λ completely uncorrelated with each other so that the total acoustic intensity defined by

$$I = \frac{c_o^3}{\rho_0} \langle \rho_a^2 \rangle$$

is the sum of the intensity produced by these jets and reads

$$I = 2\alpha \mathscr{A} D^2 \frac{c_o^3}{\rho_0} \langle \rho_{a,2D}^2 \rangle, \tag{4.12}$$

where $\rho_{a,2D}$ is the acoustic density obtained after a two-dimensional spatial integration, having the dimension of a density per metre. With (4.12) the dependence of I on the nozzle surface, here $\mathscr{A}D^2$, is recovered. Moreover, I scales with $1/x^2$ which is a characteristic of the far-field radiation. It is then convenient to use the following scaling of the acoustic intensity:

$$\mathscr{I} = 2\alpha \frac{c_o^3}{\rho_0} \langle x^2 \rho_{a,2D}^2 \rangle.$$

In the following we will refer to $\mathscr{I}$ simply as the intensity. Correspondingly, the experimental data scaling is

$$\mathscr{I} = \frac{x^2 I}{S},$$

where S is the nozzle exit surface.

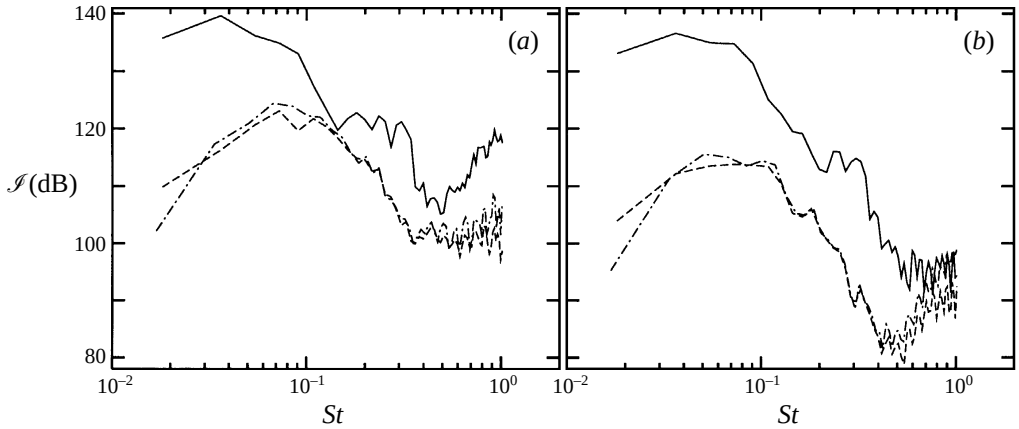

FIGURE 20. Comparison of the far-field noise spectra obtained with the three formulations of Lighthill's analogy at $M = 0.50$. (*a*) $\theta = 30°$; (*b*) $\theta = 90°$. ——, formulation (1); – – – –, formulation (2); — · —, formulation (3).

The spectra are plotted with the same scaling and with the one-third octave-band normalization. The reference level for the decibel scale is $10^{-12}\,\mathrm{W\,m^{-2}}$ for the intensity. Note that we adopt the one-third octave-band normalization because plotted with a logscale for the frequency, it gives a faithful representation of the acoustic energy distribution over the spectrum, but no averaging over each frequency band is performed. This means that the intensity at each frequency is simply weighted by the width of the band that would be centred on it. Therefore the spectrum obtained still looks like a fine-band spectrum (no peak is suppressed because of averaging over the local frequency band) but is given the one-third octave-band normalization.

Finally, it is necessary to estimate the value of α. There are very few available data on the subject but Thomas & Goldschmidt (1986) measured spanwise correlation functions in a low-Mach-number rectangular jet with an aspect ratio of 48 at various streamwise locations and obtained values of α ranging from 0.4 to 1.5. It is reasonable to take $\alpha = 1$, keeping in mind that a factor 2 change in α produces a shift of 3 dB in the acoustic intensity.

The practical details having been made clear, the spectra obtained with each formulation for the subsonic jet are shown in figure 20(*a*) for $\theta = 30°$ and figure 20(*b*) for $\theta = 90°$. Quite clearly, formulations (2) and (3) give nearly identical results while formulation (1) predicts acoustic levels higher by up to 30 dB in the low-frequency range. To understand this result one may follow the approach of Crighton (1975). The characteristic time scale of the fluctuations of the source term may be estimated locally as $l/[u]$ where l is the characteristic size of the structures and $[u]$ a velocity scale which will be specified below. Correspondingly, the retarded time scale across a structure, or a coherent eddy, is l/c_0. Suppose now that $[u]$ is much lower than c_0. Then, as a first approximation, the variations of retarded time across a structure may be neglected. Put differently, the observer 'hears' each eddy with a global delay due to propagation but with no perceptible distortion induced by the different times of emission between different parts of the eddy. Therefore, the time variations of the acoustic field are directly determined by the time variations of the source term, so that the typical frequency radiated by an eddy is $[u]/l$ and the associated wavelength is comparable to $lc_o/[u]$, which according to our assumption that $[u] \ll c_0$ is very large compared to l. This last property is expressed by saying that the sources are

acoustically compact. In this case, use of formulation (1) may be quite misleading: if retarded time effects are completely neglected in this formulation, the integral over the source volume may be transformed via the divergence theorem into a surface integral that must be zero (since there should not be any sources on this surface). This means that it is precisely the slight differences of retarded time that prevent the complete cancellation of sources. Formulation (1) is then extremely sensitive to a proper treatment of retarded time effects. There is no such problem with formulation (2) and the difference between the two formulations may be appreciated by considering (4.5) where the acoustic density given by formulation (1) is expressed as the sum of two surface integrals and one volume integral. This last integral is exactly the one that after development yields formulation (2). Thus, the difference between formulations (1) and (2) appears as the sum of two surface integrals. Theoretically of course, if the source volume is correctly defined, the surface integrals must vanish. But practically it would be dangerous to rely on the fact that the aerodynamic computational domain is large enough to ensure that these integrals are really negligible. In fact, it is seen in figure 20 that they represent a spurious radiation much more efficient than the physical one.

Now the question is to characterize the situation in which formulation (1) is not suitable for numerical estimation of the jet acoustic radiation by specifying $[u]$. In fact, for a local observer, the fluctuations of the source term are essentially due to convection and the relevant speed scale should be taken as U_c. Crighton (1975) indicates that since the subsonic convection of a frozen eddy does not produce any acoustic radiation, only the perturbations from the purely convective effect should be considered. Nevertheless, the coherent structures that develop in the flow are submitted to important distortions as they are convected and U_c/l remains a reasonable estimate for the intrinsic rate of change of structures of size l. More precisely, what matters for the preceding analysis is the rate of change seen by the observer, which means that U_c must be replaced by the apparent convection speed $U_c \cos\theta$. Of course this expression, or rather this equivalent, for $[u]$ is no longer relevant for $\theta = 90°$, when the convective effect is zero. In this case the velocity scale that should be retained is the characteristic speed of turbulent fluctuations σ_u. However, except for very high Mach numbers, still quite unusual for typical applications (say as long as $M < 3$), the condition $\sigma_u/c_0 \ll 1$ is fulfilled and the expression $U_c \cos\theta$ may be kept even for θ around 90°. Finally the parameter which determines if formulation (1) is appropriate or not is $M_c \cos\theta$, or more simply $M \cos\theta$ since M_c and M are of the same order for this purpose. Qualitatively, this means that it would be unwise to use formulation (1) at low Mach number and near $\theta = 90°$, where of course only numerical experiments may allow more precise definitions of these restrictions.

Thus, coming back to the computed results in figure 20(*a*) one must conclude that formulation (1) should be abandoned for $M = 0.5$. It may be verified in figure 20(*b*) that, in agreement with the theoretical analysis, the discrepancy between formulation (1) on one hand and formulations (2) and (3) on the other hand is even worse for $\theta = 90°$. The same comparison of the three formulations is shown in figure 21 (*a*,*b*) for the supersonic jet. This time, for $\theta = 0°$ (see figure 21*a*) the three formulations give very similar results, except perhaps in the low-frequency range. This may be understood from the fact that low-frequency components are produced by the largest structures, i.e. in the fully developed region where the velocity (hence the convection velocity) is lower than the nominal exit velocity. As expected, formulation (1) yields again an overestimated radiation at $\theta = 90°$ (see figure 21*b*).

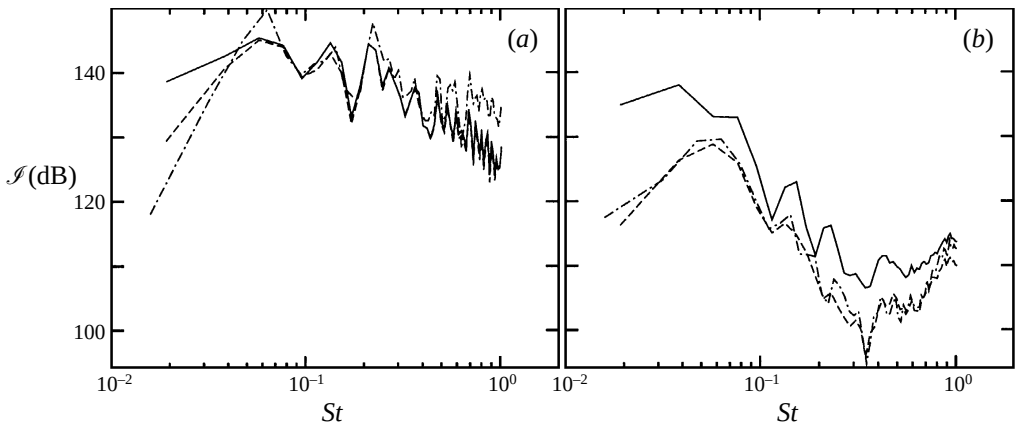

FIGURE 21. Comparison of the three formulations of Lighthill's analogy for $M = 1.33$. Same conventions as in figure 20.

A few observations can still be made from these figures. At high frequency, all the spectra tend to saturate or even to rise again. This is due to high-frequency and wavenumber aerodynamic fluctuations present in the early development of the jet shear layers. For formulation (3) which is expressed as a space–time Fourier transform, this may be assimilated into an aliasing problem, though the irregular spatial grid renders the usual theoretical analysis difficult. This spurious high-frequency radiation can be reduced for example by storing the acoustic source term with smaller time increments, which is expensive. Nevertheless it is sufficient that the significant part of the spectra is correctly evaluated, say e.g. that 95% of the energy lies under the frequency where resolution problems arise. Therefore, in the following we keep this resolution and only present the meaningful part of the spectra, that is up to the frequency where the decay of the spectrum presents a discontinuity (typically $St = 0.5$ for the formulation (2) spectrum in figure 20*b*). Correspondingly the total radiated intensity is estimated by only integrating this physical part of the spectrum.

At high frequency also, it may be noted that formulation (3) predicts levels a little higher than formulation (2) (this is clear in figure 21*b*). In fact, these two formulations are exactly equivalent, only expressed in direct or time-Fourier-transformed space. The only difference resides in the estimation of the second derivative of T_{rr} with respect to time, which is evaluated by finite differences via (4.10) in formulation (2) and which produces an exact ω^2 factor in formulation (3). It is well known that (4.10) underestimates high-frequency components by a factor $\mathrm{sinc}^2(\omega\Delta t/2)$, which explains the difference observed between the two formulations.

Finally the theoretical analysis of formulation (1) combined with numerical tests had already led Sarkar & Hussaini (1990) and Witkowska & Juvé (1994) to state that this formulation was not suitable for numerical estimation of the noise produced by decaying isotropic homogeneous turbulence with very low turbulent Mach number. It is shown here for a realistic jet flow configuration that formulation (1) is inappropriate for the study of the noise radiated by subsonic jets and for supersonic jets around $\theta = 90°$. Therefore it is definitely not convenient for a computational approach, even at high Mach number. In contrast, formulation (3) is the simplest to implement. It also allows a simple geometrical interpretation in $(\boldsymbol{\kappa}, \omega)$-space. Thus formulation (3) is retained for all acoustic computations for the two subsonic and supersonic jets.

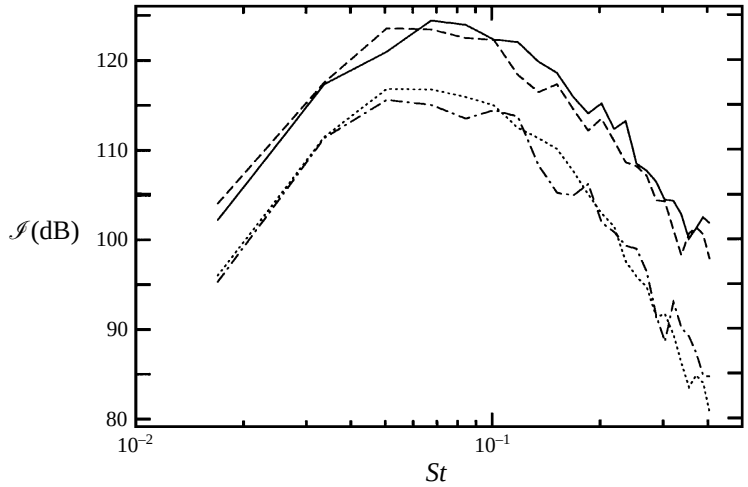

FIGURE 22. Influence of the amplitude of the excitation β, where β is defined in (3.1), on the computed radiated noise at $M = 0.50$. ——, $\theta = 30^\circ$ and $\beta = 0.005$; – – – –, $\theta = 30^\circ$ and $\beta = 0.0025$; —·—, $\theta = 90^\circ$ and $\beta = 0.005$; ·····, $\theta = 90^\circ$ and $\beta = 0.0025$.

Note that other formulations of Lighthill's analogy exist, such as those of Ribner (1964) or Howe (1975). The first tends to enlarge the spatial distribution of the source term, while the second is in practice limited to low-speed flows, and these formulations are therefore less suitable for numerical calculations.

5. Acoustic results

The computational approach described previously is now used to obtain acoustic field estimates. These results will be interpreted in the light of experimental data.

5.1. *The aerodynamic excitation*

It is first important to check that the aerodynamic excitation does not influence acoustic computations. As explained in §3, the transverse velocity profile in the nozzle is perturbed with an excitation described by (3.1), the intensity of which is determined by the parameter β. It is first verified that the computed spectra do not show any rise in the excitation band (from $St = 0.2$ to 0.5). Moreover, a simple and decisive test is to modify the amplitude of the excitation to see how the radiated noise is affected. Thus, figure 22 displays the computed acoustic spectra obtained for the subsonic jet at $\theta = 30^\circ$ and $\theta = 90^\circ$ for two different values of β: $\beta = 0.005$ which is the value adopted everywhere else and $\beta = 0.0025$. If there was a direct connection between the excitation introduced in the aerodynamic calculations and the estimated acoustic intensity, there would be a homogeneous shift of 6 dB between the two curves at each angle. Obviously, there is no such variation. The small differences as β is changed are not of constant sign all over the spectrum and may well be explained as statistical fluctuations which would disappear by averaging the results over a larger number of samples. Of course, the same observation could have been made on the aerodynamic spectra.

5.2. *The subsonic jet*

Very few experiments deal with the noise produced by high-aspect-ratio rectangular jets. However, in the subsonic range, Kouts & Yu (1974) made some acoustic

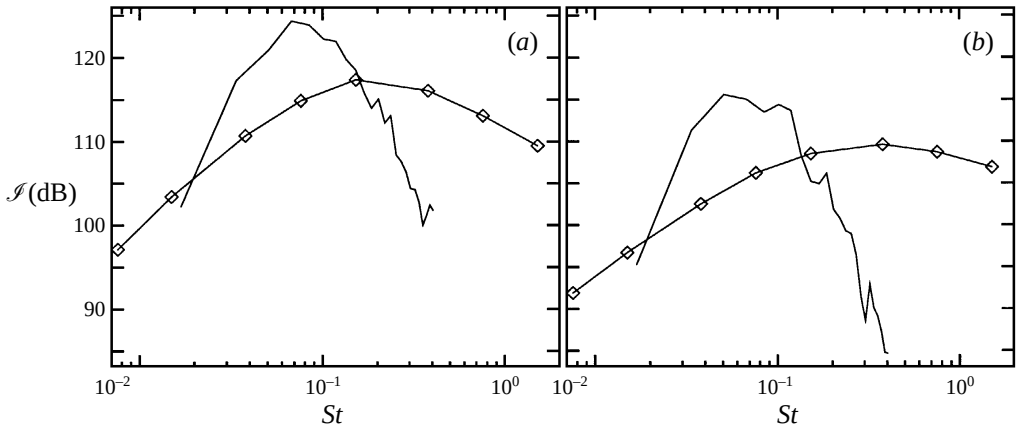

FIGURE 23. Acoustic radiation from the subsonic jet ($M = 0.50$). (*a*) $\theta = 30°$; (*b*) $\theta = 90°$. ——, Present computation; —◇—, experimental data for a rectangular jet at $M = 0.54$ with $\mathscr{A} = 10$ (Kouts & Yu 1974).

measurements on a rectangular jet with an aspect ratio of 10 for Mach numbers ranging from 0.3 to 0.7 and provide a rather complete set of data for $M = 0.54$ which is the case closest to our computed jet at $M = 0.50$. Other measurements relevant to the subsonic jet have been reported by Olsen, Gutierrez & Dorsch (1973). The jet is rectangular, the aspect ratio $\mathscr{A} = 69$ and $M = 0.50$. Unfortunately this reference does not contain spectra at different angles of emission.

Therefore, the computed spectra obtained for the subsonic jet at $\theta = 30°$ and $\theta = 90°$ are compared in figure 23(*a*,*b*) with the data of Kouts & Yu (1974). Of course an exact match was not to be expected because of the various levels of approximation used in the calculation. More specifically two separate problems may be identified in these plots. First the level of the numerical prediction is too high by up to 10 dB at certain frequencies. This can be explained essentially by the fact, underlined in §3, that the level of the computed aerodynamic fluctuations and hence of the acoustic source term, is overestimated. Consider for example that since the acoustic intensity depends quadratically on the acoustic fluctuation level, a shift of 10 dB may be accounted for by a factor 3 on the coherent structures level. The second point is more important and relates to the spectral contents of the computed radiation. Thus, the high-frequency part of the experimental spectra, say for $St > 0.2$, is essentially missing in the numerical estimates. Correspondingly, the decay of the computed spectra at high frequency is much steeper.

To explain this, it is necessary to discuss the origin of the high-frequency acoustic radiation from subsonic jets. The very small coherent structures arising near the jet nozzle constitute one possible source of this noise. This follows the simple idea that the frequency of the radiated noise is directly linked to the characteristic frequency of the eddies emitting it. However, this assumption is contradicted numerically: it has been verified that an aerodynamic computation using a grid especially refined near the nozzle provides a precise representation of the small structures in the beginning of the shear layers but that the radiated noise spectra are hardly modified. In fact, a simple time representation of the noise generation mechanism is not sufficient and the answer lies in the distribution of the acoustic source term in the two-dimensional wavenumber–frequency space. This distribution, evaluated numerically, is presented in figure 24(*a*,*b*) for the subsonic jet. The similarity with sketches imagined e.g. by

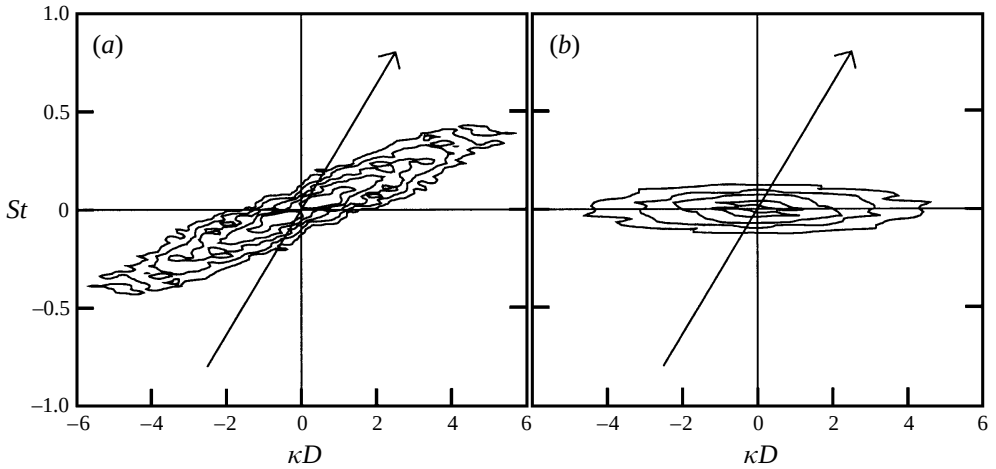

FIGURE 24. Contours of the space–time power spectral density of Lighthill' source term for $M = 0.50$. (a) $\theta = 0°$; (b) $\theta = 90°$. Five contours are drawn from 10 dB under the maximum attained in the plane for $\theta = 0°$, in increments of -8 dB. The arrow represents the sonic line.

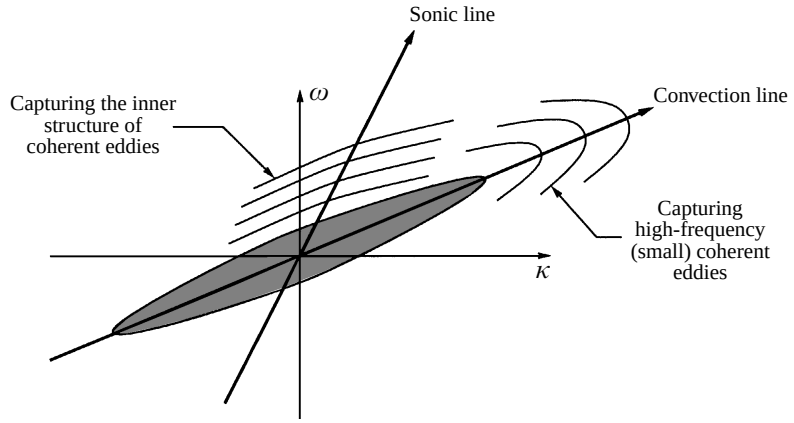

FIGURE 25. Interpretation in the (κ, ω)-plane of the origin of the high-frequency radiation in a subsonic jet. Conventions of figure 18 are adopted.

Ffowcs Williams (1963) or with the one shown in figure 18 is striking. The dominant (κ, ω)-components of the source term are clearly localized along a straight line, which as explained in §4 is interpreted as the convection line. As expected, the slope of the convection line is zero for $\theta = 90°$ (see figure 24b).

Now what happens when high-frequency coherent structures are captured is shown in figure 25: these eddies are subjected to the mean flow convective effect and the distribution of the source term is extended along the convection line, where it brings no contribution at all to the radiated noise. Only the largest coherent structures (with lowest characteristic wavenumber) may be direct contributors. Pursuing this analysis, it appears that the high-frequency acoustic radiation is due to the source term components that are away from the convection line, i.e. rather to internal structures that modify the main convection effect and broaden the localization of the source term around the convection line. This gives another point of view on the well-known fact that the acoustic efficiency of subsonic jets is very poor: noise may be produced

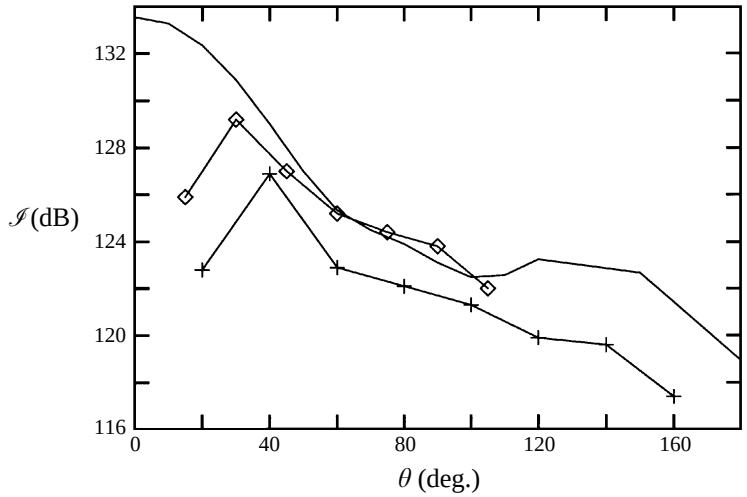

FIGURE 26. Acoustic directivity for the subsonic jet ($M = 0.50$). ——, Present computation; —◇—, experimental data for a rectangular jet at $M = 0.54$ with $\mathscr{A} = 10$ (Kouts & Yu 1974); —+—, experimental data for a rectangular jet at $M = 0.55$ with $\mathscr{A} = 69$ (Olsen *et al.* 1973).

only by a low-intensity part of the aerodynamic fluctuations, acting as a perturbation of the global jet development.

As a consequence, it is not possible to solve this problem using SDM. In fact, the present model only captures coherent structures radiation. The inner fine-grained turbulence within the coherent eddies which should be represented to obtain broad-band radiated noise spectra is not part of the coherent motion. Practically, the limit between what is computed and what is modelled in SDM is not adjustable and the computation is roughly independent of the grid employed, except of course very near the nozzle where the size of the first structures to appear is determined by the minimum mesh spacing. In this sense, and it is one of our important conclusions, subsonic jet noise, at least up to $M = 0.50$, may not be predicted in a satisfactory manner with only the contribution of large-scale coherent motion.

Despite the fact that only the low-frequency part of the radiated noise may be represented, the acoustic directivity is seen in figure 26 to be correctly estimated. The reader should not be confused by the fact that the level of the computed directivity compares so well with the experimental data: this agreement is mainly due to the cancellation of two errors, namely the overestimation of the acoustic level at low frequency and the lack of high-frequency radiation. However, the decrease of the acoustic emission as the polar angle θ increases is well captured, consistently with the (κ, ω)-space analysis presented in §4. At small angles of observation, the experimental directivities decrease because acoustic waves are refracted by the mean flow. As explained previously, this phenomenon may not be represented by Lighthill's analogy, so that it is perfectly normal that its effects do not appear in the numerical calculation. Finally, the small rise of the computed directivity for $\theta > 110^\circ$ is a spurious phenomenon due to signal processing problems in the region where the actual acoustic integral of the source term is so low that it is easily perturbed by numerical errors.

5.3. *The supersonic jet*

If, as shown in the following, the numerical estimation of supersonic jet noise is easier, the validation by experiments on rectangular jets is even more difficult because it is

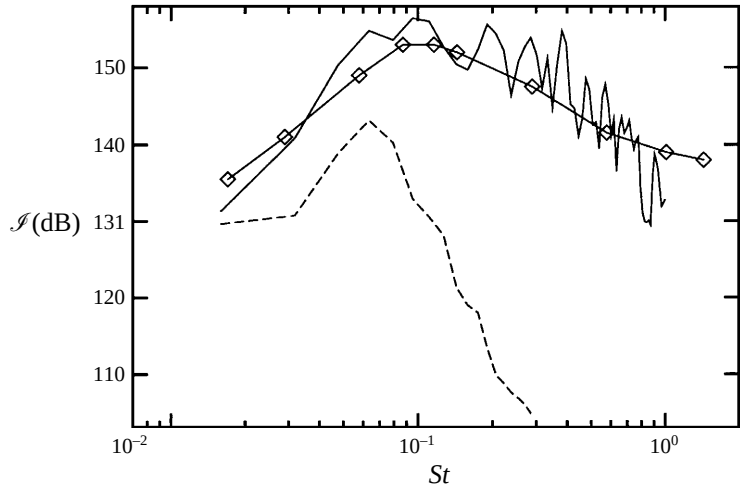

FIGURE 27. Acoustic radiation from the supersonic jet ($M = 1.33$). ——, Present computation at $\theta = 22.5°$; – – – –, $\theta = 90°$; —◇—, experimental data at $\theta = 22.5°$ for a rectangular jet at $U_J/c_0 = 1.33$, $M = 1.66$ and $\mathscr{A} = 1.5$ (Seiner *et al.* 1986).

technically almost impossible to obtain a supersonic fully expanded rectangular jet. We here use measurements of Seiner, Ponton & Manning (1986) (also documented in Ponton, Manning & Seiner 1986) where the case of interest is a rectangular jet at Mach number 1.66 with a nozzle exit aspect ratio of 1.5. This is an unheated jet and the ratio U_J/c_0, which is the essential parameter (rather than M) as regards supersonic jet noise, may be estimated to be 1.33, while our computed jet corresponds to $M = 1.33$ and $T_J = T_0$. As a first approximation, the temperature effect between the two numerical and experimental jets may be reduced to a simple shift in the acoustic level, according to the well-known dimensional law

$$\mathscr{I} \propto \rho_J^2 U_J^8.$$

Therefore, the computed acoustic intensities should be expected to be about 4 dB below the experimental ones.

The computed spectra are shown in figure 27 for $\theta = 22.5°$ and $\theta = 90°$. For $\theta = 22.5°$, the spectrum measured by Seiner *et al.* (1986) is also indicated. As 4 dB should separate the two spectra at $\theta = 22.5°$, the collapse of the curves must be considered as a numerical overestimation by 4 dB. This is a minor discrepancy, in view e.g. of the simplicity of the three-dimensional normalization of the two-dimensional acoustic computations. Besides, it can be explained as above by the overestimation of the coherent structure level. This overestimation has been shown to be less pronounced than for the subsonic jet, explaining the better prediction of the acoustic level. More important and in complete contrast with the preceding case, the shape of the spectrum is in excellent agreement with the experiment. The oscillations that perturb the computed spectrum would of course be completely smoothed out by a real one-third octave-band averaging.

The explanation for this agreement may again be drawn from the source term (κ, ω)-space distribution, which is plotted in figure 28. This time the convection line is much closer to the sonic line and most of the aerodynamic fluctuations contribute to the sound field. In other words the whole spectrum of the radiated noise may be accounted for by the coherent structures contribution. In fact, this is true for

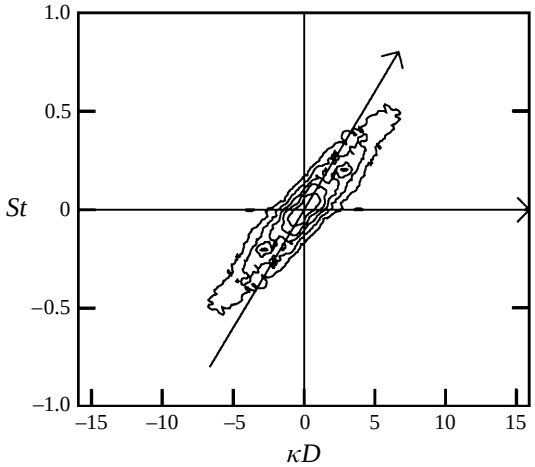

FIGURE 28. Contours of the space–time power spectral density of Lighthill's source term for $M = 1.33$ at $\theta = 0°$. Five contours are drawn from 15 dB under the maximum attained in the plane, in increments of −10 dB. The arrow represents the sonic line.

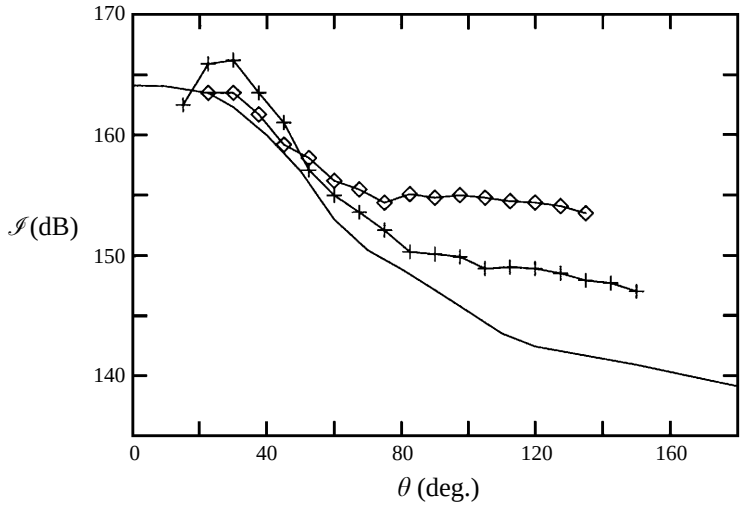

FIGURE 29. Acoustic directivity for the supersonic jet ($M = 1.33$). ——, Present computation; —◇—, experimental data for a rectangular jet at $U_J/c_0 = 1.33$, $M = 1.66$ and $\mathscr{A} = 1.5$ (Seiner *et al.* 1986); —+—, experimental data for a circular jet at $U_J/c_0 = 1.37$ and $M = 1.33$ (Tanna *et al.* 1976).

low angles of emission. When θ increases, the convection line moves away from the sonic line and a situation similar to the subsonic one is recovered. Thus, there are no reliable experimental data for the spectrum radiated at 90° but the experimental spectral density is certainly broader than what is observed in figure 27.

This may be seen also in the directivity, displayed in figure 29. Measurements by Tanna, Dean & Burrin (1976) for a circular jet at Mach number 1.33 with $U_J/c_0 = 1.37$ are also indicated and the relatively higher acoustic level on the rear arc ($\theta > 90°$) for the experimental rectangular jet is due to shock-associated noise. Thus, the rectangular jet of Seiner *et al.* (1986) is not really perfectly expanded and the circular jet directivity is more representative of what should be expected from

the computations. Apart from the refraction drop-off at small angles, the numerical directivity is satisfactory in the forward arc and tends to decrease too fast at higher angles of observation. This stems from the fact that only the low-frequency part of the spectra is correctly estimated. Note also that the vertical range is different between figures 26 and 29 and that the steepening of the directivity as the Mach number increases, which was also predicted from the (κ, ω)-space interpretation of Lighthill's analogy, is well captured.

6. Conclusions

This study focuses on the assumption that most of the noise radiated by high-Reynolds-number free shear flows is determined by the large-scale coherent motion. It is shown here that the use of classical theories combined with modern numerical methods yields an efficient computational approach to address this problem.

One original feature of this work is the use of semi-deterministic modelling (SDM) which specifically accounts for the aerodynamic coherent motion. SDM may be derived in principle from most classical turbulence closures and is obtained here from the classical $k-\epsilon$ model. At present, the main difficulty of this implementation of SDM is the lack of a well-documented calibration. Thus, the ratio of the coherent fluctuations level to the total turbulence level, hence the amplitude of the coherent structures, depends on the choice of the viscosity constant C_μ. The determination of C_μ poses problems which are somewhat analogous to those found in devising Smagorinsky-like subgrid-scale models for LES. Nevertheless the computation of a realistic unsteady jet flow remains a challenging problem to which SDM brings a satisfactory solution.

The far sound field radiated by the computed coherent structures is suitably evaluated from Lighthill's analogy. In contrast with other computational aeroacoustic (CAA) approaches, such as Kirchhoff's formulation or direct numerical simulation, it does not require a complete representation of the compressible near field. For this reason also, near-field propagation effects, namely refraction, may not be captured. Despite this restriction the present approach is well suited to applications of practical interest. It has been verified that at least for subsonic flows, the different integral formulations of Lighthill's theory are not equally adapted to numerical estimation. The formulation retained here is the one expressed in a space–time Fourier transformed plane. Besides being adequate whatever the Mach number, it leads to a geometrical interpretation and to further understanding of the radiation process. This interpretation greatly helps the acoustic results analysis. Thus, the high-frequency part of the acoustic radiation tends to be missing when the contribution of the coherent structures does not dominate the sound field. From this work, we may deduce that this occurs for subsonic jets, at least up to Mach number 0.50 and for supersonic jets when the angle of observation is far from the angle of maximum emission. More precisely, in this case, the high-frequency radiation is due to smaller eddies inside the largest ones, that perturb their main convective character. Yet directivity effects are always correctly captured, even though the absolute acoustic level is at present too high, due to an overestimation of the coherent structure amplitude by SDM. The present analysis indicates that for *subsonic jets the acoustic radiation is not dominated by the direct contribution of large-scale coherent structures.* Roughly speaking, at Mach number 0.50, the acoustic frequencies represented by the computation lie between $St = 0.02$ and $St = 0.2$ while the experimental spectra occupy a band ten times larger from $St = 0.02$ to $St = 2$. Yet half of the energy is located below $St = 0.2$

and from this point of view we are close to having captured the 'dominant part' of the radiated noise. This result may be considered in relation to observations by Witkowska, Brasseur & Juvé (1995) who show that noise radiated by low Reynolds number isotropic homogeneous turbulence is dominated by the contribution of eddies about three times smaller than energy-containing scales. At this stage, it would be interesting to know if the use of conventional large-eddy simulation (LES) may provide better results. With LES, it is theoretically possible to adjust the maximum spatial wavenumber accessible in the computation. With a sufficiently fine grid, it must be possible to capture a part of the inner structure of the large eddies, which would allow a greater portion of high-frequency acoustic radiation to be obtained. Yet, first tests performed with Smagorinsky's model support the idea that to broaden the acoustic spectra it is necessary to refine the aerodynamic computational grid in the same proportion, which is very expensive. Besides, it should be kept in mind that two-dimensional computations become less adequate as finer spatial scales are calculated. Of course, the problem is easier to handle as the Mach number is increased and high-subsonic or transonic jets may be treated more reasonably.

In contrast with most CAA approaches, this combination of SDM with Lighthill's analogy yields results that are close enough to available experimental data to make the comparison informative. For the plane jet case treated here though, it is necessary to model the transverse correlation scale to get three-dimensional acoustic results from two-dimensional computations. The axisymmetric configuration is experimentally much better documented and would permit direct comparisons. Yet, a two-dimensional axisymmetric computation of a round jet is questionable since in this case even the large-scale coherent motion is known to be generally three-dimensional. Thus full three-dimensional computations could be considered in the near future. For the treatment of the high-frequency part of the acoustic radiation in subsonic jets, the approach described here may also be coupled to a more classical statistical model which would account for the radiation of smaller, presumably more homogeneous, turbulent spatial scales.

Finally a referee has brought to our attention the problem of the sound originating inside the jet pipe or immediatly at the nozzle lip, rather than produced by the turbulent fluctuations of the external flow. The nature of the mechanism by which this contribution affects the global radiated noise is still a problem and the question is open of whether the present approach is suitable. However the precise configuration of the nozzle is of great importance for this problem and the flow computation should provide a reliable, probably fine-scale, representation of the exit region, including at least a portion of the nozzle lip. These demanding constraints have still to be satisfied but it may then be interesting to tackle this issue with a computational approach.

We wish to thank Professor D. Vandromme for providing the code used for aerodynamic computations. This work is part of the PhD dissertation of the first author, who is greatly indebted to SNECMA for its support, monitored by H. Joubert. Computer resources and support from EDF is also gratefully acknowledged.

REFERENCES

Barre, S., Quine, C. & Dussauge, J. P. 1994 Compressibility effects on the structure of supersonic mixing layers: experimental results. *J. Fluid Mech.* **259**, 47–78.

Béchara, W., Lafon, P., Bailly, C. & Candel, S. 1995 Application of a $k-\epsilon$ model to the prediction of noise for simple and coaxial free jets. *J. Acoust. Soc. Am.* **97**, 3518–3531.

Bishop, K. A., Ffowcs Williams, J. E. & Smith, W. 1971 On the noise sources of the unsuppressed high-speed jet. *J. Fluid Mech.* **50**, 21–31.

Blake, W. K. 1986 *Mechanics of Flow-Induced Sound and Vibration. Vol. I General Concepts and Elementary Sources.* Academic.

Bogdanoff, D. W. 1983 Compressibility effects in turbulent shear layers. *AIAA J.* **21**, 926–927.

Brown, G. L. & Roshko, A. 1974 On density effects and large structure in turbulent mixing layers. *J. Fluid Mech.* **64**, 775–816.

Buell, J. C. & Huerre, P. 1988 Inflow/outflow boundary conditions and global dynamics of spatial mixing layers. *Center for Turbulence Research, Proc. of the Summer Program*, pp. 19–27.

Colonius, T., Lele, S. K. & Moin, P. 1993 Boundary conditions for direct computation of aerodynamic sound generation. *AIAA J.* **31**, 1574–1582.

Crighton, D. G. 1975 Basic principles of aerodynamic noise generation. *Prog. Aerospace Sci.* **16**, 31–96.

Crow, S. C. & Champagne, F. H. 1971 Orderly structure in jet turbulence. *J. Fluid Mech.* **48**, 547–591.

Dimotakis, P. E. 1986 Two-dimensional shear-layer entrainment. *AIAA J.* **24**, 1791–1796.

Ffowcs Williams, J. E. 1963 The noise from turbulence convected at high speed. *Phil. Trans. R. Soc. Lond.* A **225**, 469–503.

Ffowcs Williams, J. E. & Kempton, A. J. 1978 The noise from the large-scale structure of a jet. *J. Fluid Mech.* **84**, 673–694.

Ffowcs Williams, J. E. & Maidanik, D. L. 1965 The Mach wave field radiated by supersonic turbulent shear flows. *J. Fluid Mech.* **21**, 641–657.

Giles, M. B. 1990 Nonreflecting boundary conditions for Euler equation calculations. *AIAA J.* **28**, 2050–2058.

Goebel, S. G. & Dutton, J. C. 1991 Experimental study of compressible turbulent mixing layers. *AIAA J.* **29**, 538–546.

Goldstein, M. E. & Rosenbaum, B. 1973 Effects of anisotropic turbulence on aerodynamic noise. *J. Acoust. Soc. Am.* **54**, 630–645.

Ha Minh, H. 1994 Order and disorder in turbulent flows: their impact on turbulence modelling. *Osborne Reynolds centenary symposium, UMIST, Manchester, 24 May.*

Ha Minh, H., Viegas, J. R., Rubesin, M. W., Vandromme, D. D. & Spalart, P. 1989 Physical analysis and second-order modelling of an unsteady turbulent flow: the oscillating boundary layer on a flat plate. *Proc. Seventh Intl Symp. on Turbulent Shear Flows, Stanford University, Stanford, CA.*

Howe, M. S. 1975 Contributions to the theory of aerodynamic sound, with application to excess jet noise and the theory of the flute. *J. Fluid Mech.* **71**, 625–673.

Huerre, P. & Monkewitz, P. A. 1990 Local and global instabilities in spatially developing flows. *Ann. Rev. Fluid Mech.* **22**, 473–537.

Hussain, A. K. M. F. 1983 Coherent structures-reality and myth. *Phys. Fluids* **26**, 2816–2850.

Hussain, A. K. M. F. & Reynolds, W. C. 1970 The mechanics of an organized wave in turbulent shear flow. *J. Fluid Mech.* **41**, 241–258.

Johansson, S. H., Davidson, L. & Olsson, E. 1993 Numerical simulation of vortex shedding past triangular cylinder at high Reynolds number using a $k-\epsilon$ turbulence model. *Intl J. Numer. Methods Fluids* **16**, 859–878.

Jones, W. P. & Launder, B. E. 1972 The prediction of laminarization with a two-equation model of turbulence. *Intl J. Heat Mass Transfer* **15**, 301–314.

Kouts, C. & Yu, J. C. 1974 Far noise field of a two-dimensional subsonic jet. *AIAA Paper* 74-44.

Lau, J. C., Morris, P. J. & Fisher, M. J. 1979 Measurements in subsonic and supersonic free jets using a laser velocimeter. *J. Fluid Mech.* **93**, 1–27.

Laufer, J. 1974 On the mechanism of noise generation by turbulence. *Omaggio a Carlo Ferrari*, pp. 451–464. Libreria Editrice Universitaria Levrotto & Bella, Torino.

Laufer, J. & Yen, T.-C. 1983 Noise generation by a low-Mach-number jet. *J. Fluid Mech.* **134**, 1–31.

Lepicovsky, J., Ahuja, K. K., Brown, W. H. & Burrin, R. H. 1985 Coherent large-scale structures in high Reynolds number supersonic jets. *NASA Contractor Report* 3952.

Liepmann, H. W. 1952 Aspects of the turbulence problem. Part II. *Z. Angew. Math. Mech.* **3**, 407–426.

LIGHTHILL, M. J. 1952 On sound generated aerodynamically. I. General theory. *Proc. R. Soc. Lond.* A **211**, 564–587.

LIU, J. T. C. 1974 Developing large-scale wavelike eddies and the near jet noise field. *J. Fluid Mech.* **62**, 437–464.

LIU, J. T. C. 1988 Contributions to the understanding of large-scale coherent structures in developing free turbulent shear flows. *Adv. Appl. Mech.* **26**, 183–305.

LONGMIRE, E. K. & EATON, J. K. 1994 Active open-loop control of particle dispersion in round jets. *AIAA J.* **32**, 555–563.

MCCORMACK, R. W. 1981 A numerical method for solving the equations of compressible viscous flow. *AIAA Paper* 81-0110.

MCINNES, J. M., CLAUS, R. W. & HUANG, P. G. 1989 Time-dependent calculation of a forced mixing layer using a k—ϵ turbulence model. *Proc. Seventh Intl Symp. on Turbulent Shear Flows, Stanford University, Stanford, CA.*

MCLAUGHLIN, D. K., MORRISON, G. L. & TROUTT, T. R. 1975 Experiments on the instability waves in a supersonic jet and their acoustic radiation. *J. Fluid Mech.* **69**, 73–95.

MCLAUGHLIN, D. K., MORRISON, G. L. & TROUTT, T. R. 1977 Reynolds number dependence in supersonic jet noise. *AIAA J.* **15**, 526–532.

MITCHELL, B. E., LELE, S. K. & MOIN, P. 1995 Direct computation of the sound from a compressible co-rotating vortex pair. *J. Fluid Mech.* **285**, 181–202.

MOORE, C. J. 1977 The role of shear-layer instability waves in jet exhaust noise. *J. Fluid Mech.* **80**, 321–367.

MORRIS, P. J. 1977 Flow characteristics of the large scale wave-like structure of a supersonic round jet. *J. Sound Vib.* **53**, 223–244.

MUMFORD, J. C. 1982 The structure of the large eddies in fully developed turbulent shear flows. Part 1. The plane jet *J. Fluid Mech.* **118**, 241–268.

OLSEN, W. A., GUTIERREZ, O. A. & DORSCH, R. G. 1973 The effect of nozzle inlet shape, lip thickness, and exit shape and size on subsonic jet noise. *AIAA Paper* 73-187.

PAPAMOSCHOU, D. & ROSHKO, A. 1988 The compressible turbulent shear layer: an experimental study. *J. Fluid Mech.* **197**, 453–477.

PHILLIPS, 0. M. 1960 On the generation of sound by supersonic turbulent shear layers. *J. Fluid Mech.* **9**, 1–28.

POINSOT, T. J. & LELE, S. K. 1992 Boundary conditions for direct simulations of compressible viscous flows. *J. Comput. Phys.* **101**, 104–129.

PONTON, M. K., MANNING, J. C. & SEINER, J. M. 1986 Far-field acoustics of supersonic rectangular nozzles with various throat aspect ratios. *NASA Tech. Mem.* 89002.

RIBNER, H. S. 1964 The generation of sound by turbulent jets. In *Advances in Applied Mechanics* (ed. H. L. Dryden & T. von Karman), pp. 103–182. Academic.

RIBNER, H. S. 1969 Quadrupole correlations governing the pattern of jet noise. *J. Fluid Mech.* **38**, 1–24.

SAMIMY, M. & ELLIOTT, G. S. 1990 Effects of compressibility on the characteristics of free shear layers. *AIAA J.* **28**, 439–445.

SARKAR, S. & HUSSAINI, M. Y. 1993 Computation of the acoustic radiation from bounded homogeneous flows. In *Computational Aeroacoustics* (ed. J. C. Hardin & M. Y. Hussaini), pp. 335–355. Springer.

SEINER, J. M., MCLAUGHLIN, D. K. & LIU, C. H. 1982 Supersonic jet noise generated by large-scale instabilities. *NASA Tech. Paper* 2072.

SEINER, J. M., PONTON, M. K. & MANNING, J. C. 1986 Acoustic properties associated with rectangular geometry supersonic nozzles. *AIAA Paper* 86-1867.

SHIH, C., KROTHAPALLI, A. & GOGIENI, S. 1992 Experimental observations of instability modes in a rectangular jet. *AIAA J.* **30**, 2388–2394.

TAM, C. K. W. 1991 Jet noise generated by large-scale coherent motion. In *NASA Reference Publication 1258,* Vol. 1 (ed. H. H. Hubbard), pp. 311–390.

TAM, C. K. W. & BURTON, D. E. 1984 Sound generated by instability waves of supersonic flows. Part 2. Axisymmetric jets. *J. Fluid Mech.* **138**, 273–295.

TAM, C. K. W. & MORRIS, P. J. 1980 The radiation of sound by the instability waves of a compressible plane turbulent shear layer. *J. Fluid Mech.* **98**, 349–381.

TANNA, H. K., DEAN, P. D. & BURRIN, R. H. 1976 The generation and radiation of supersonic jet

noise. Vol. III. Turbulent mixing noise data. *Air Force Aero-Propulsion Laboratory, Tech. Rep.* 76-65.

Thomas, F. O. & Goldschmidt, V. W. 1986 Structural characteristics of a developing turbulent planar jet. *J. Fluid Mech.* **163**, 227–256.

Witkowska, A., Brasseur, J. G. & Juvé, D. 1995 Numerical study of noise from stationary isotropic turbulence. *16th AIAA Aeroacoustics Conf. Proc., München, 12–15 June*, pp. 255–263.

Witkowska, A. & Juvé, D. 1994 Numerical estimation of noise generated by homogeneous and isotropic turbulence. *C. R. Acad. Sci. Paris* **318**, 597–602.